The management of imaging dose during image-guided radiotherapy: Report of the AAPM Task Group 75

Martin J. Murphy
Department of Radiation Oncology, Virginia Commonwealth University, Richmond, Virginia 23298

James Balter
Department of Radiation Oncology, University of Michigan, Ann Arbor, Michigan 48109

Stephen Balter
Departments of Medicine and Radiology, Columbia University Medical Center, New York, New York 10021

Jose A. BenComo, Jr.
Department of Radiation Physics, M.D. Anderson Cancer Center, Houston, Texas 77030

Indra J. Das
Department of Radiation Oncology, University of Pennsylvania School of Medicine, Philadelphia, Pennsylvania 19104

Steve B. Jiang
Department of Radiation Oncology, University of California, San Diego, La Jolla, California 92093

C.-M. Ma
Department of Radiation Oncology, Fox Chase Cancer Center, Philadelphia, Pennsylvania 19111

Gustavo H. Olivera
Department of Medical Physics, University of Wisconsin, Madison, Wisconsin 53706

Raymond F. Rodebaugh
St. Joseph's Hospital, Phoenix, Arizona 85013

Kenneth J. Ruchala
TomoTherapy, Inc., Madison, Wisconsin 53717

Hiroki Shirato
Department of Radiology, Hokkaido University Hospital, Hokkaido, Japan

Fang-Fang Yin
Department of Radiation Oncology, Duke University Medical Center, Durham, North Carolina 27710

(Received 8 January 2007; revised 5 July 2007; accepted for publication 22 July 2007; published 26 September 2007)

Radiographic image guidance has emerged as the new paradigm for patient positioning, target localization, and external beam alignment in radiotherapy. Although widely varied in modality and method, all radiographic guidance techniques have one thing in common—they can give a significant radiation dose to the patient. As with all medical uses of ionizing radiation, the general view is that this exposure should be carefully managed. The philosophy for dose management adopted by the diagnostic imaging community is summarized by the acronym ALARA, i.e., as low as reasonably achievable. But unlike the general situation with diagnostic imaging and image-guided surgery, image-guided radiotherapy (IGRT) adds the imaging dose to an already high level of therapeutic radiation. There is furthermore an interplay between increased imaging and improved therapeutic dose conformity that suggests the possibility of optimizing rather than simply minimizing the imaging dose. For this reason, the management of imaging dose during radiotherapy is a different problem than its management during routine diagnostic or image-guided surgical procedures. The imaging dose received as part of a radiotherapy treatment has long been regarded as negligible and thus has been quantified in a fairly loose manner. On the other hand, radiation oncologists examine the therapy dose distribution in minute detail. The introduction of more intensive imaging procedures for IGRT now obligates the clinician to evaluate therapeutic and imaging doses in a more balanced manner. This task group is charged with addressing the issue of radiation dose delivered via image guidance techniques during radiotherapy. The group has developed this charge into three objectives: (1) Compile an overview of image-guidance techniques and their associated radiation dose levels, to provide the clinician using a particular set of image guidance techniques with enough data to estimate the total diagnostic dose for a specific treatment scenario, (2) identify ways to

reduce the total imaging dose without sacrificing essential imaging information, and (3) recommend optimization strategies to trade off imaging dose with improvements in therapeutic dose delivery. The end goal is to enable the design of image guidance regimens that are as effective and efficient as possible. [DOI: 10.1118/1.2775667]

TABLE OF CONTENTS

I. INTRODUCTION

In an editorial in the *British Journal of Radiology*, Aird[1] addresses the issue of dose delivered to the rest of the body during external-beam radiotherapy. This concomitant ("extra-target") dose includes external linac head leakage and scatter, internal direct and scattered therapy dose outside the target volume, as well as nontherapeutic doses from imaging for planning and delivery. Total concomitant dose is increasing steadily with the introduction of more imaging procedures to the treatment process. However, much of this exposure is only qualitatively monitored, and some is not monitored at all. Aird maintains that because this cumulative extra-target dose has a negative biological effect even within the context of radiotherapy, it is important that the radiation therapy community assess its cost and benefit. This task group was formed to contribute to this process by compiling data on concomitant imaging dose and identifying ways for it to be reduced or optimized.

Image-guided radiotherapy (IGRT) makes use of many different imaging techniques, using modalities ranging from portal imaging to fluoroscopy to megavoltage cone-beam CT and following regimens as simple as a single setup image or as complex as intrafraction tumor tracking.[2–5] The total imaging radiation dose experienced by a patient can include multiple CT scans for planning, pretreatment fluoroscopic studies to analyze tumor motion, and a series of interfraction and intrafraction images for target localization. The delivery of this dose can be spread out over several weeks during conventional radiotherapy or confined to a short time for hypofractionated radiotherapy and radiosurgery. Imaging dose can be concentrated at the skin or distributed throughout the anatomical volume of interest. Given these circumstances it is no longer safe to consider the dose from only one imaging procedure at a time or to assume that the cumulative imaging dose is negligible compared to the therapeutic dose.

Data for the dose delivered by the various radiographic imaging modalities being used during radiation therapy are presently scattered widely through the literature, making it

difficult to estimate the total dose that the patient will receive during a particular treatment scenario. This problem is compounded by the fact that equipment configurations (such as source/patient distance) developed for radiotherapy guidance often differ significantly from their diagnostic imaging counterparts and by the fact that many of these imaging configurations have only recently come into clinical use. Finally, the different imaging modalities deliver very different spatial distributions of dose resulting in significantly different physiological risks. This makes it difficult to synthesize a complete picture of the patient's exposure. To manage total imaging dose one must first know what it is; therefore the primary goal of this task group report is to collect into one place enough data to allow the clinical practitioner to make an informed estimate of the total imaging dose delivered to the patient during the complete treatment process. Although precise dose estimation in radiology and radiation therapy is a complex and sometimes controversial problem we consider that the data in this report are adequate for about a factor of 2 estimate of air kerma and effective dose. This degree of precision should allow clinicians to make reasonably informed judgments about their image-guidance procedures.

I.A. The current and emerging uses of imaging during radiation therapy

Until the late 1990s, imaging for radiotherapy was confined to the acquisition of a CT study for treatment planning, one or two simulation images for setup, and one or two portal images at the beginning of selected treatment fractions. This practice was based on the assumption that the patient's anatomy exposed to the treatment beam was tolerant of alignment errors of the order of 5–15 mm. The development of conformal 3D therapy, intensity-modulated radiotherapy (IMRT), and frameless stereotactic radiosurgery has reduced the alignment error tolerance to a few millimeters for targets that move and deform during the treatment process. Image guidance was introduced to deal with these more challenging treatment scenarios. Image-guided radiotherapy now involves multiple imaging procedures for planning, simulation, setup, and intrafraction monitoring.

This task group is concerned with transmission-type radiographic imaging using x rays. Emission-type imaging (nuclear medicine, PET, SPECT), although entering into wider use during the planning process, involves a fundamentally different type of dosimetry than transmission radiography and hence has not been included in the scope of this report. Nevertheless, anytime it is used, the clinician should consider its contribution to the total dose. Ultrasound and magnetic resonance imaging, which are also entering into widespread use for radiotherapy, do not involve ionizing radiation and thus do not fall within the scope of this report.

During the planning process, CT is almost always used to contour the target and critical structures. CT can now be done in either axial, spiral, or cone-beam mode. PET and SPECT images are sometimes fused with the planning CT to enhance specificity and sensitivity to the tumor and involved organs.

If the organs can move during respiration then additional imaging is used to characterize the motion. Tumor motion margins due to respiration or other influences have conventionally been assessed prior to treatment via multiple CT studies (fast, slow, breathhold, etc.).[6] The development of breathing-correlated CT (now often referred to as 4D CT) allows one to obtain a temporal sequence of 3D image studies that chronicle the anatomy during the breathing cycle. This technique is especially useful to accommodate and analyze breathing motion. However, a 4D CT binned into ten breathing phases that approximately preserve 3D CT image quality will be acquired at a total dose that is at least several times that of a single high-quality CT and potentially as much as the cumulative dose from ten individual CTs.

If organ motion is going to be accommodated in a planning target volume (PTV) margin then the CT can provide the margin information. If the treatment plan involves active motion management during treatment, then pretreatment fluoroscopic studies may be required to characterize the trajectory of the moving tumor. These trajectories form the basis for setting up a motion management scheme using either breathholding, beam gating, or active target tracking.

Image-guided patient setup requires simulation images in addition to the planning CT study. These images, which define the patient treatment position, have traditionally been obtained via film or electronic imaging using a kV simulator that is separate from the planning CT. Modern virtual CT simulation allows one to calculate digitally reconstructed radiographs (DRRs) directly from the planning CT to use as the simulation images. This avoids the additional imaging dose and positioning error contributed by a separate simulation procedure and is therefore a positive development in the management of concomitant dose.

Patient setup at the beginning of each fraction can now be done either with portal imaging, diagnostic x-ray imaging, or in-room CT (both conventional and cone-beam, kilovoltage, and megavoltage). In-room CT allows soft-tissue targets to be precisely aligned within the coordinate frame of the beam delivery system and can in principle provide setup images at the start of every fraction. Cone-beam CT uses either the therapy beam itself or a gantry-mounted kilovoltage source and detector, thus eliminating the need for an independent CT scanner in the treatment room. TomoTherapy[7,8] provides megavoltage fan-beam CT integrated with the treatment delivery system.

Intrafraction motion of the target (due to either patient movement or internal physiological functions such as breathing) can be monitored by dual radiographic x-ray imaging, fluoroscopy, or portal imaging using an electronic portal imaging device (EPID) in *cine* mode.

Respiratory motion during treatment presents the most difficult target alignment problem and is presently being addressed via a number of management and tracking techniques (see for example Bortfeld and Chen[9] and the references therein, and Keall *et al.*[10]). Many of these motion management techniques, including beam gating and dynamic tracking, require both pretreatment analysis of the motion trajectories via diagnostic fluoroscopy and/or 4D CT and in-

trafraction imaging to monitor the motion. At the present time, the most precise (and at the same time the most dose intensive) real-time monitoring is done via dual orthogonal fluoroscopes that continually image the treatment site throughout the fraction.[11] Therefore real-time management of respiratory motion potentially involves the most radiographic exposure of all image-guided radiotherapy procedures.

The insertion of both brachytherapy seeds and HDR sources is done under fluoroscopic and/or CT guidance. This has much in common with fluoroscopy used during surgical procedures, and the cumulative diagnostic dose can be considerable.

I.B. The need for imaging dose management

Exposure to ionizing radiation presents two potential health hazards—the risk of deterministic injury such as skin burns and cataracts and the probabilistic (stochastic) risk of inducing cancer or genetic defects. The danger of deterministic injury from prolonged fluoroscopy[12] has been graphically demonstrated by several instances of severe burns following poorly monitored image-guided surgical interventions.[13] Stochastic risk enters more broadly as a result of concomitant dose from both the therapy beam and from the imaging procedures. Concern over concomitant dose from the therapy beam itself has been broadened to include not only LINAC leakage but also secondary radiation (including neutrons) generated from the larger number of monitor units (MUs) that are characteristic of IMRT.[14–16]

Even though radiation therapy patients are already being exposed to very high and localized doses of radiation, the additional radiation from imaging has an associated risk and should be kept low.[16] Dose minimization, however, must be within a context of relative cost versus benefit that will vary from patient to patient. A 20 year old being treated via image-guided radiosurgery for an arterio-venous malformation assumes a stochastic risk from imaging radiation that is fundamentally different from a 70 year old being treated via image-guided IMRT for prostate cancer. Children are ten times more radiation sensitive than adults, and girls are more sensitive than boys.[17,18] Therefore imaging dose should be managed on a case-by-case basis.

Concerns over the risk associated with concomitant exposure during radiotherapy already account for the limits on leakage and background from the primary therapy beam: "The absorbed dose rate due to leakage radiation (excluding neutrons) at any point outside the maximum sized useful beam at the normal treatment distance shall not exceed 0.2% of the absorbed dose rate on the central axis at the treatment distance."[19] For a 60 Gy treatment delivered over 30 fractions there will be less than 120 mGy of megavoltage radiation leakage. A conventional portal film requires 50–100 mGy of megavoltage dose, while an EPID can require 10–50 mGy per image. If daily AP and lateral EPID portal images are acquired for setup over 30 fractions,[20,21] the total concomitant dose can be significantly more than the limit for background dose from the beam and can increase the therapeutic dose by several percent. While such an aggressive schedule of portal imaging may not be common, it illustrates the imaging dose budget that must be considered when high targeting precision is required. Similarly, one CT study (30–50 mGy) per fraction to assist daily setup would deliver a total of 500–1500 mGy of diagnostic-energy radiation to the patient. Although the energy and field of exposure differ for beam leakage, portal imaging, and CT, making direct comparison problematic, the imaging doses are clearly not negligible. The health and safety considerations that underlie the limit on therapy beam background dose should therefore be considered as relevant for imaging exposures as well.

It is especially important for practitioners of IGRT to recognize that most of the imaging techniques they employ will deliver a qualitatively different kind of radiation distribution than the therapy beam itself. In particular, planar kilovoltage imaging presents the possibility of deterministic skin injury because the maximum dose is at the skin's surface. Therefore entrance skin dose is one standard measure of diagnostic imaging dose. One should also be aware that both the direct and scattered treatment beam adds skin dose, thus pushing the total skin dose closer to the levels associated with deterministic injury.

Other users of interventional radiographic imaging, e.g., image-guided surgery and intraoperative fluoroscopy, are becoming increasingly aware of the cumulative dose the patient receives during the procedure and are exploring ways to reduce the radiation dose without giving up valuable imaging information.[22]

I.C. Dose management

It is not within the charge of this task group to recommend total allowable imaging doses, as this requires radiological analysis that is beyond the expertise of the group. What this report provides is dose information and guidelines to manage the dose in the spirit of the ALARA convention.[23]

We identify three steps in the dose management process: (1) Assessment, (2) reduction, and (3) optimization. Assessment consists of estimating the total imaging dose that the patient will receive during a given IGRT treatment regimen. The primary purpose of this task group report is to provide the necessary data to make this assessment, quantified in units that allow approximate intercomparison and summing among modalities. Reduction consists of refining the imaging regimen or technique to eliminate a dose that does not contribute to the information needed to plan, set up, or monitor the patient. Diagnostic imaging technologies adapted for IGRT can deliver an unnecessary dose that is either outside the useful field of view (FOV) or beyond the minimum sampling frequency needed to document patterns of target motion. For example, if a patient is undergoing respiratory-gated treatment during which the target position is monitored fluoroscopically, the temporal motion of the target can be adequately observed at a sampling rate considerably less than the fluoroscopic standard of 30 frames per second. Finally, the imaging regimen can be optimized by recognizing

that as imaging increases, therapeutic dose to healthy tissue is reduced, but at the expense of more diagnostic dose elsewhere. At some point, a cost/benefit balance will be reached. However, these trade-offs will be highly individualized to the treatment site and the treatment protocol, making it impractical for this task group to formulate generalized quantitative optimization procedures.

I.D. Evaluating imaging dose

When analyzing imaging dosimetry during radiation therapy we must recognize three fundamental distinctions. The first is between local dose and integral dose. Dose per se in units of Gy (Joules/kg) is a local (point) measure of the energy deposited per unit of mass by ionizing radiation. Dose can be reduced only by decreasing the fluence (i.e., decreasing the intensity and/or duration) of radiation reaching a particular point at the surface of or within the patient. Integral dose is the total dose integrated over the exposed mass (volume) of the anatomy and can be reduced by either decreasing the fluence or decreasing the area/volume irradiated. The effective management of radiological imaging should (in the spirit of ALARA) keep both dose and integral dose to a minimum level.

The second distinction is between planar and axial imaging. In planar imaging the dose to the patient is greatest at the skin surface nearest to the source and falls off progressively as the radiation transits the body to the image detector. Axial imaging, which is the basis for CT, differs in that the dose, by design, is distributed nearly uniformly throughout the imaged volume to produce 3D images of uniform cross-sectional quality. Therefore dose in planar imaging is concentrated at the skin while dose for tomography is distributed more in the manner of 3D radiation therapy. Furthermore, the planar imaging dose has a gradient across organs along the path from entrance to exit. This distinction is most pronounced for kilovoltage (diagnostic) modalities where for a planar image the falloff in dose from entrance to exit can be a factor of 100 to 1000. Therefore a planar diagnostic imaging modality that delivers 10 mGy of air kerma to the imaging isocenter exposes the patient in a very different way from a CT scan that delivers 10 mGy of axial air kerma, and the two quantities should not be casually treated as comparable or interchangeable. This distinction persists at megavoltage energies, where a planar portal image distributes dose differently than a megavoltage CT. Finally, the entrance air kerma defined for planar radiography does not include backscatter from the patient, while the generally used CT dose quantity CT dose index ($CTDI_{100}$), being a measure of internally deposited dose in a phantom, does include scatter.

The third distinction is between kilovoltage and megavoltage imaging. Absorbed dose is the meaningful quantity for estimating the biological effects of radiation. At diagnostic imaging energies the range of secondary electrons is short enough that the tissue kerma and absorbed dose are approximately the same even at the skin surface. For soft and superficial tissues the conversion factor for tissue to air kerma is close enough to one to allow use of air kerma in estimates of biological risk from exposure to kilovoltage photons. As the energy of the photon beam increases, though, the range of the secondary electrons increases. This leads to regions (primarily air/tissue interfaces) where dose buildup is not in equilibrium and the local tissue kerma is significantly different from the locally absorbed dose. At megavoltage photon energies neither air nor tissue kerma is a useful indicator of absorbed dose (and thus biological risk) at the skin or other interfaces that are not in electronic equilibrium.

Given these distinctions we must deal with several different quantities that are commonly used to report dose. For varieties of planar kilovoltage imaging we have entrance skin dose, i.e., air kerma, in units of mGy. Entrance skin dose does not include backscatter. For kilovoltage CT we have air kerma on the axis of rotation in mGy, with or without scatter included, i.e., CTDI in air ($CTDI_{air}$) and in a phantom ($CTDI_w$). The use of entrance air kerma for planar imaging and $CTDI_w$ for axial imaging conforms to the AAPM convention for defining reference dose values for diagnostic radiology (AAPM Task Group 7 report[24]). Megavoltage imaging is usually quantified in either monitor units (MU) or cGy of absorbed dose. To monitor the integral dose we have the dose area product (DAP) for planar imaging and the dose length product (DLP) for axial (i.e., CT) imaging.

There are fundamental differences in the distribution of radiation from the various imaging modalities used during radiotherapy, making it difficult to compare and combine the doses. The prevailing convention for making these comparisons involves the conversion of the delivered dose to an equivalent whole-body exposure that characterizes the resulting health detriment.[25] The comparison concept is "effective dose," defined by Jacobi[26] as "the mean absorbed dose from a uniform whole-body irradiation that results in the same total radiation detriment as from the non-uniform, partial-body irradiation in question." In this context "radiation detriment" refers to stochastic risk; effective dose is the standard metric for estimating stochastic risk. The unit for effective dose is the milli-Sievert (mSv). In theory the effective dose is defined as in Eq. (1a)

$$E = \sum_T w_T H_T, \tag{1a}$$

where the H_T are the average organ doses to tissue T for a particular exam, and the w_T are tissue weighting factors that represent the relative radiation sensitivities of the organs. Equation (1a) is evaluated for each exam and patient type to obtain a conversion factor in units of delivered dose. In practice, effective dose from a particular imaging procedure is obtained by multiplying the delivered imaging dose, reported as air kerma, entrance skin exposure, CTDI, absorbed dose, or MU, by the conversion factor that is specific to the patient's age, sex, and the anatomical region that is imaged. These conversion factors (and thus the whole basic concept of effective dose) are based on estimations of stochastic risk obtained by combining weighted averages of the exposure risk for all organs in the imaging field of view. To make a meaningful estimate of risk from the total imaging dose the contributions from each modality should first be converted to

effective dose and then summed. Section IV of this report will summarize the basic process for converting imaging exposures to effective dose and provide selected example scenarios. The evaluation of deterministic risk such as skin injury is more problematic because it occurs at locations where the absorbed dose from higher-energy imaging photons has not reached buildup equilibrium.

In discussions of imaging dose management during radiotherapy one frequently hears the imaging dose compared to either the direct or concomitant dose delivered by the treatment beam itself. While this comparison is a fundamentally important consideration it is typically done by naively equating imaging dose in cGy with treatment beam, scatter, and leakage expressed also in cGy. In reality the comparison process is more complicated. As with the different diagnostic imaging modalities, the comparison should be made using units of effective dose. However, as we have already mentioned, effective dose is based on estimates of biological effect integrated over the entire patient volume, which in turn requires detailed knowledge of the energy spectrum and spatial geometry of the incident radiation. Radiation treatment geometries are much more varied and patient-specific than imaging geometries. Furthermore, therapeutic doses and dose gradients are very different from diagnostic imaging, which potentially influences the tissue weighting factors used in computing effective dose. Finally, there is some question whether the population-based biological effect models used for risk assessment in diagnostic imaging are appropriate to the highly selective subset of patients undergoing radiation therapy.[1] For these reasons the estimation of effective dose during actual treatment, although possible in principle, has rarely been attempted. Therefore the task group considers that it is not yet practical to quantitatively combine its evaluation of total imaging dose with the evaluation of total concomitant therapeutic dose. Because this comparison appears to be of great interest to the radiation therapy community, we consider that theoretical and/or empirical estimates of effective dose from the therapy beam during treatment should be made.

I.E. An important note on terminology and units

In this document we use the word "exposure" to describe the process of delivering radiation (as in "the exposure of the patient to imaging radiation") and the word "dose" for the amount of radiation received by the patient. We point out this distinction because in radiological literature there is an old but not entirely obsolete practice of using the word "exposure" both qualitatively in our sense and also as a quantifiable amount of radiation, defined differently than dose. We never use "exposure" in the sense of a radiation quantity.

The radiation therapy community uses Gy or cGy as the standard unit for expressing dose, while the diagnostic imaging community uses mGy. Although this document is intended primarily as a resource for radiation therapy, its subject is imaging dose. Therefore it will follow the diagnostic imaging convention and express local dose in mGy. Adhering to this convention is especially important when dealing with the conversion of local dose to effective dose because that conversion is conventionally given in units of $\mathrm{mSv/mGy\,cm^2}$. The radiation therapy practitioner is therefore cautioned to double check all estimates of imaging dose for consistency in units, especially when the dose has initially been expressed in rads or millirads and when portal imaging doses are being analyzed.

II. IMAGING MODALITIES AND DOSES

Although there is considerable variation among precise equipment geometries and dose details for imaging modalities used during IGRT, the dose to the patient is still determined mainly by the required image quality, the attenuation characteristics of the imaged anatomy, and the imaging duty cycle rather than the equipment details. Thus for each modality the dose to the patient for each treatment scenario is approximately the same regardless of whose equipment is in use. This allows some generalization from the data available for particular IGRT setups. For each modality this section summarizes the standard geometry (source/patient/detector distance, field of exposure), the imaging duty cycle (duration/frequency), and the dose characteristics (fluence, spectra) for selected examples of equipment. The following section discusses the use of this equipment in representative IGRT applications.

II.A. Portal imaging

Portal imaging has progressed from the use of film as the imaging detector, through screen/camera imagers and liquid ionization chambers, to solid-state flat-panel detectors. Although there are institutions still equipped with and using the older detector systems, the flat-panel imager is emerging as the new standard detector for portal imaging in IGRT. We therefore focus our discussion of portal imaging on the use of solid-state detectors, although it should be understood that the film systems, being less efficient, require higher doses.

The nominal source/isocenter distance is that of the treatment machine, i.e., 100 cm. Source/detector distances are variable from 120 to 150 cm. The level of exposure used to image a particular treatment site is typically varied by integrating dose over multiple acquisition frames of fixed duration. The duration of each frame is typically fixed as an integral number of MUs. Cumulative doses to acquire a single image using amorphous silicon panels range from 1 to 5 MU for most users.

For those LINAC systems that permit the setting of an arbitrary portal image exposure level (i.e., not in integer number of MU) it is possible to acquire images with less than 1 MU. There are instances where this can provide an adequate image. Consequently this capability represents an important means to reduce total portal imaging dose, which is especially important for scenarios that involve daily imaging.

FIG. 1. CyberKnife image-guided radiosurgery system with robot-mounted linac, patient couch, dual orthogonal imaging detectors in the floor, and dual x-ray imaging sources mounted at the ceiling. (Image courtesy of Accuray, Inc.)

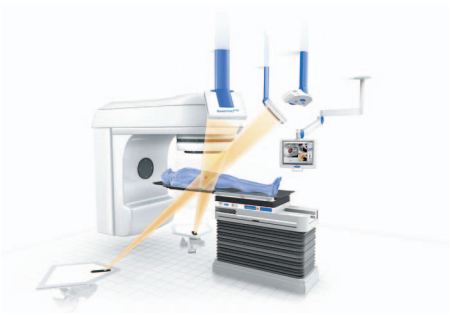

FIG. 2. The Brainlab ExacTrac configuration of dual orthogonal x-ray sources and detectors. (Image courtesy of BrainLaB AG.)

II.B. Radiography

Diagnostic x-ray imaging provides better contrast over shorter exposure intervals than portal imaging and is rapidly being adopted as an improvement for patient setup and tracking during treatment. The usual implementation involves either dual kilovoltage x-ray sources and solid-state flat-panel detectors mounted permanently to the floor and ceiling of the treatment room or a source/detector system mounted to the gantry arm for rotation around the patient.

II.B.1. CyberKnife

The CyberKnife (Accuray, Sunnyvale, CA) is an image-guided robotic system for radiosurgery and stereotactic radiotherapy. The integrated imaging system determines the location of the treatment site based on either anatomical or artificially placed fiducial landmarks and then directs the LINAC pointing system at the treatment site via a real-time control loop. It is capable of repeated imaging during treatment. The CyberKnife system utilizes two ceiling-mounted kilovoltage sources and two floor-mounted amorphous silicon flat-panel detectors arranged to provide orthogonal views on either side of the patient, as shown in Fig. 1. The source-to-isocenter separation is 265 cm. The isocenter-to-detector separation is 65 cm. The detector active area is 25 cm square.

The source/patient entrance distance is nominally 250 cm for cranial radiosurgery and 240 cm for body radiosurgery. The source has 2 mm of aluminum filtration and is collimated to a square field that is nominally 17 cm $\times$ 17 cm at the patient. The source collimator is telescopic, which allows the field size to be adjusted. Table I summarizes the ranges of technique and approximate entrance dose per image for targets at various body locations (data provided by Accuray, Inc, Sunnyvale, CA). For the abdominal and pelvic sites the patient's body weight strongly influences the technique required to get good images. The *Synchrony* technique refers to a special function of the CyberKnife system that tracks thoracic and abdominal treatment sites that move with breathing; the technique for these sites uses a shortened exposure period to reduce motion blurring. The total exposure for each target position determination has contributions from two orthogonal imaging projections, with a doubling of dose wherever the collimated source fields overlap at the patient.

TABLE I. Measured planar radiographic entrance dose levels per image for the CyberKnife image-guided radiosurgery system.

Site	kV	mA	ms	mAs	mGy
Cranium and C-spine	105–125	100	100	10	0.25
T-spine	120–125	100–150	100–125	10–20	0.25–0.50
L-spine	120–125	100–200	100–150	10–30	0.25–0.75
Sacrum	120–125	100–300	100–300	10–90	0.25–2.00
Synchrony	120–125	100–300	50–75	5–22.5	0.10–0.50

II.B.2. BrainLab Novalis ExacTrac system

The imaging dose from the radiographic imaging system (ExacTrac) that forms part of the BrainLab Novalis patient positioning system (BrainLab, Feldkirchen, Germany) has been measured at the Henry Ford Hospital in Detroit, Michigan.[27] The x-ray imagers are amorphous flat-panel detectors $20.5 \times 20.5/\mathrm{cm}^2$. As with the CyberKnife, the Novalis system has dual orthogonal x-ray sources and detectors fixed within the treatment room. This imaging system is configured with x-ray sources in the floor and detectors mounted at the ceiling, forming an oblique imaging geometry (Fig. 2). The source-isocenter distance is 234 cm, and the isocenter-detector distance is 128 cm. Table II summarizes the measured entrance dose levels for two imaging applications—head and neck targeting and thoracic/lumbar spine targeting. The sources typically illuminate a $13.5 \times 13.5\ \mathrm{cm}^2$ FOV at the patient, corresponding to the full FOV of the detectors, but this is adjustable. All images are obtained in pairs so the total effective dose is summed from two imaging projections.

TABLE II. Measured planar radiographic entrance dose levels for the BrainLab Novalis image-guided radiosurgery system [from the Henry Ford Hospital (Ref. 27)].

Site	kV	mA	ms	mAs	mGy
Cranium and C-spine	120	125	100	12.5	0.335
Body	140	125	125	15	0.551

II.B.3. Gantry-mounted kilovoltage imaging

Both Elekta (Stockholm, Sweden) and Varian Medical Systems (Palo Alto, CA) have introduced gantry-mounted kV imaging systems (Synergy XVI and On-Board Imager OBI, respectively) that can be used in radiographic, fluoroscopic, and cone-beam CT modes. When used in radiographic mode to acquire AP and lateral alignment radiographs the dose to the patient is approximately 1–3 mGy per image,[28] depending on technique.

II.C. Computed tomography

CT is and will remain the primary imaging mode for radiotherapy treatment planning[29–32] because it displays soft tissue structures well enough for organ delineation, it reveals the bony landmarks used for patient setup, it allows for the generation of DRRs for patient positioning, and it directly measures the electron densities needed for dose computation during the planning process. However, as the variety of imaging techniques used during image-guided radiotherapy increases, it is easy to overlook the dose from conventional CT. This oversight is perhaps a carryover from diagnostic imaging practice, which did not fully recognize or appreciate the exposure levels from CT until the late 1980s.[33] When exposure levels from all modes of diagnostic imaging were surveyed it was found that

> "CT therefore represents by far the largest contribution to the radiation exposure of the population from diagnostic medical sources."[33]

Specifically, although it represents only 4% of all examinations in Germany, it contributes 35% of the total diagnostic dose delivered to patients.[33]

CT can now be performed in axial and spiral mode using single and multislice fan-beam arrays, and in cone-beam mode using 2D dimensional detector arrays. In the technological evolution from single detector/single slice scanners to spiral, multislice, and cone-beam machines, any reduction in dose for a single exam achieved via increased speed or efficiency has been more than offset by the resultant tendency among clinicians to increase the amount of image information collected, by increasing the scan length, decreasing the slice thickness, and/or performing oversampled scans to monitor fast real-time processes such as breathing. Consequently, CT exposure levels for a particular exam have in fact tended to increase over the years.[33]

The tendency in the diagnostic community to exploit technical advances in CT by expanding the scope and complexity of its use (and thus increasing the resulting exposure) has been mirrored in the radiotherapy community—today, multiple CTs are acquired to define breathing-related treatment margins, phase-correlated CT is being introduced to monitor breathing in real time, CT imaging is being integrated with treatment machines to allow 3D patient setup using anatomical landmarks, and repeated scans during the treatment process are being considered to adapt treatment plans to changes in patient anatomy over time.

II.C.1. Estimating the computed tomography dose index (CTDI)

CT dose depends on the manner in which the scan is acquired and is most often given as the CTDI in units of mGy. This is the dosimetric expression used by the AAPM Task Group 8 report on standardized methods for measuring diagnostic x-ray doses[34] and in the AAPM Task Group 7 report on reference values for radiology.[24]

The CTDI represents the total dose (with or without scatter—see below) deposited at a point within a single scan slice during a complete exam and allows for the fact that slices up and downstream from a particular slice will contribute dose to the point in question. It is computed by integrating the dose delivered along the entire axis of rotation during a single axial rotation of the scanner:

$$\mathrm{CTDI} = (1/h)\int_{-\infty}^{\infty} D(z)dz, \tag{2a}$$

where $D(z)$ is the dose at a position z along the axis of rotation, and h is the nominal slice thickness.

All of the details of dose overlap and summing at a particular point in space are captured by the quantity CTDI. To calculate an accurate estimate requires detailed knowledge of the scanning methodology for a given machine, including beam collimation, profile, and penumbra, overlapping or spacing of the slices, spiral versus axial geometry, filtration, etc. For a factor of 2 or better level of accuracy one should use tabulated doses for specific exams, such as those given in Table VII of this report and in references such as Nagel.[33]

Equation (2a) is a theoretical definition of CTDI. For practical purposes, one uses the measured quantity CTDI_{100}:

$$\mathrm{CTDI}_{100} = (1/h)\int_{-50}^{50} K_{\mathrm{air}}(z)dz, \tag{2b}$$

where K_{air} is the air kerma. This is obtained in the clinical setting with an ionization chamber that integrates the dose of a single slice of an axial scan over a length of 100 mm. Measurements are made in the center and at eight equally spaced peripheral locations around the center circumference of a cylindrical Plexiglas phantom of either 16 cm (head) or 32 cm (torso) diameter. The peripheral measurement points are at a depth of 1 cm from the surface. CTDI_w is the weighted average of the CTDI_{100} measurements at the center and the peripheral locations in the phantom. CTDI_w is an approximation of the average dose of a cross section of a patient's body and is calculated as follows:

$$\mathrm{CTDI}_w = [2/3\mathrm{CTDI}_{100}(\mathrm{Periphery}) + 1/3\mathrm{CTDI}_{100}(\mathrm{Center})]. \tag{2c}$$

The measurement of CTDI_{100} includes backscatter from the phantom. If the measurement of center axial dose defined in Eq. (2b) is made without a phantom, then one obtains the axial dose in the absence of scatter (dose-free-in-air), or $\mathrm{CTDI}_{\mathrm{air}}$. The axial dose-free-in-air is directly comparable to entrance air kerma, and has units of mGy.

Equations (2a) and (2b) assume a pitch of 1 for the ratio of table feed to slice thickness, i.e., the slices do not overlap or have space between them. If the pitch is less than 1, then the CTDI does not represent the total effective dose, because dose at a particular point is superimposed from neighboring overlapping slices. The general quantity introduced to account for this superposition (or spreading out) of dose is the multiple scan average dose (MSAD), which for nonspiral scans is estimated from the CTDI by

$$\mathrm{MSAD} = (nh/I)\mathrm{CTDI}, \tag{2d}$$

where n is the number of scans (i.e., slices), h is the nominal slice thickness (mm), and I is the table advance in millimeters during one gantry rotation. For spiral scans at a pitch p, MSAD is related to the CTDI according to

$$\mathrm{MSAD} = (1/p)\mathrm{CTDI}. \tag{2e}$$

If dose has been calibrated specifically in terms of weighted CTDI (Eq. (2c)) then the corresponding MSAD is called effective CTDI:

$$\mathrm{CTDI}_{w,\mathrm{eff}} = \mathrm{MSAD}_w = (1/p)\mathrm{CTDI}_w. \tag{2f}$$

One also sees the quantity denoted "volume CTDI" ($\mathrm{CTDI}_{\mathrm{vol}}$), which is the same as CTDI_w.

The DLP is an approximation of the dose from an entire CT examination. DLP is calculated by

$$\mathrm{DLP} = (\mathrm{CTDI}_w) \times (\mathrm{Scan\ Length}). \tag{2g}$$

To allow for variability in mAs for any given exam a normalized ${}_n\mathrm{CTDI}$ can be defined in units of mGy per mAs. The following formula provides a general means to estimate, within a factor of 2, the delivered axial dose in the absence of scatter, expressed in units of the mAs technique set up for a particular examination:

$$D_{\mathrm{air}} = {}_n\mathrm{CTDI}_{\mathrm{air}} \cdot Q[\mathrm{mGy}], \tag{2h}$$

where the ${}_n\mathrm{CTDI}_{\mathrm{air}} \approx 0.20$ mGy per mAs, and Q=(current) $\times$(time) per slice in mAs.[33] Notice that the product of current and time is for one slice, not for the full duration of the imaging sequence, because the radiation exposure moves progressively through the anatomy as the patient is scanned.

II.C.2. Doses for typical CT exams

Diederich *et al.*[35] indicate an axial air kerma ($\mathrm{CTDI}_{\mathrm{air}}$) of 30–50 mGy for a typical multislice chest CT of an adult of average size. Table VII in Sec. IV A 2 provides a more detailed summary of CT doses for a variety of examinations.

II.C.3. Respiration-correlated 4D CT

Modern radiation therapy treatment planning must contend with organ motion during both the CT imaging and treatment processes. The most problematic source of motion is due to respiration, which is fast enough to cause artifacts even in a fast CT. Furthermore, motion must be assessed prior to treatment to determine either an appropriate motion margin or parameters for a motion compensation method. To address both of these problems, respiration-correlated CT (also called 4D CT) has been developed. Respiration-correlated CT acquires the equivalent of several very fast CTs over one breathing cycle by actually acquiring a slow, oversampled CT during which the data are time tagged to indicate the particular moment in the breathing cycle at which the measurement is made. After the scan is complete the time-tagged data are sorted into time bins to reconstruct a temporal sequence of 3D CT images, each representing a short interval of the breathing cycle.

There are two basic acquisition methods. One is to make a single continuous helical scan at a pitch much less than 1 and sort the sinogram data according to physiological signals or time stamps. The other method is to make an axial scan in *cine* mode—i.e., acquire multiple images of a single group of slices without table motion, while time tagging the reconstructed slices to correlate with breathing phase, then increment the table position and acquire another set of multiple images. In both cases data are acquired for the equivalent of multiple CT scans, and the dose is consequently greater than for a single conventional scan.

To maintain standard diagnostic image quality, respiration-correlated CTs would need to be acquired at the same technique setting as a conventional single scan, in which case the total dose for a scan acquired in a single slow table feed at pitch $p<1$ can be estimated from Eq. (2d). Keall *et al.*[36] describe the acquisition of 4D thoracic CT data using the continuous helical method at standard chest technique with a pitch $p=0.125$ for which the total effective dose is eight times the dose from a single conventional scan. In this scenario the axial air kerma for a respiration-correlated thoracic CT will be in the range of 250–400 mGy. Low *et al.*[37] describe a 4D thoracic CT acquisition using the axial *cine* method in which 15 time-tagged images, each of 0.50 s duration, were acquired at each table position at a technique of 120 keV and 80 mA. This corresponds to 40 mAs per slice per image. Standard CT technique for an adult chest scan is in the range of 200–250 mAs per slice. The 4D images were acquired at a significantly lower technique and correspond to a total dose approximately equivalent to three conventional scans, or about 100 mGy.

II.C.4. CT-on-rails

In one approach (Primatom Siemens Oncology Care Systems Group, Concord, CA) a conventional CT scanner is placed in the treatment room, either on the same couch axis as the LINAC gantry, or on an orthogonal axis to the gantry. A single couch serves the CT scanner and the beam delivery system. The couch is first rotated into alignment with the CT scanner to acquire a pretreatment CT. The CT scanner is mounted on rails so that it, rather than the couch, moves in the axial direction relative to the patient to collect a volumetric scan. This CT is used to establish the time-of-treatment target configuration. The couch is then rotated back into line with the gantry for treatment. This geometry is illustrated schematically in Fig. 3.

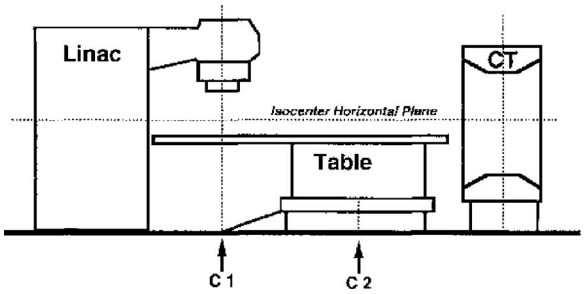

FIG. 3. The schematic geometry for a CT-on-rails system showing the two rotation axes of the couch: C1 being the conventional rotational axis with respect to the Linac isocenter and C2 being the axis to rotate the couch into alignment with the CT scanner, which moves on rails along the scan axis.

II.C.5. kV Cone-beam CT

An alternative approach is to collect CT images using a modified conventional treatment gantry. One version of this is to use the EPID system, or an enhanced detector, for MV cone beam CT.[38] Another variation is to add additional apparatus to generate kilovoltage cone beam CT.[39,40] Figure 4 illustrates the generic cone-beam CT geometry for image-guided radiotherapy. Kilovoltage cone beam CT systems made by Elekta (XVI) and Varian (On-board Imager) both include a diagnostic kV source and a flat-panel detector, mounted on opposite sides of the patient and orthogonal to the LINAC beam. In both systems, the x-ray tube and detector can retract when not in use to reduce detector exposure to the detrimental effects of the treatment beam. The integrated LINAC/CT system unveiled by Siemens (Primatom) has been adapted to perform cone beam kVCT as well, but using an in-line, rather than orthogonal geometry.[41] The flat-panel detector is mounted below the LINAC head in the accessory tray, and the x-ray source is mounted near the EPID. Kilovoltage cone beam CT for radiation therapy has also been investigated using mobile C-arm gantries. This implementation is still under study and is not yet commercially available.

The dose delivered by the Elekta XVI kV cone-beam CT has been measured by Islam *et al.*[42] The tube was operated at 120 kVp and the complete scan technique was 660 mAs. The tube energy spectrum was hardened by adding 2 mm of Al and 0.1 mm of Cu filtration. The detector sensitive area was 41 cm×41 cm, and the source/detector distance was 155 cm. Torso and head doses were simulated using 32 cm diameter and 16 cm diameter cylindrical water phantoms.

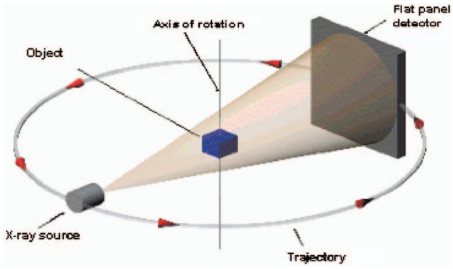

FIG. 4. Conventional geometry for cone-beam CT.

The typical doses at the center and surface of the body phantom were 16 and 23 mGy, while for the head phantom the center and surface doses were 30 and 29 mGy, respectively. These measurements followed the standard CT dose measurement protocol outlined in Sec. II C.

A CBCT pelvic exam dose level of 25 mGy for 400 projections at 130 kVp and 1.2 mAs per projection has been reported by Amer *et al.*[43] using the Elekta system. This dose level is comparable to the measurements of Islam *et al.*[42] when corrected for differences in x-ray technique (kVp and mAs), and scan protocol (i.e., number of projections). Cossmann *et al.*[44] report doses of 30–80 mGy from the Varian OBI system for 900 projections, a 48 cm field of view, and a scan length of 17 cm. Measurements of the Varian OBI system at Virginia Commonwealth University using a bowtie filter, 125 kVp, and the low-dose technique (616 projections at 0.4 mAs) gave center and surface doses of 15 mGy for a 16 cm cylindrical (head) phantom. For the standard dose technique (616 projections at 2 mAs) the head phantom dose was 74 mGy at the center and 72 mGy at the surface. Finally, Endo *et al.*[45] have measured both local and effective dose for kV CBCT (see Sec. IV A 3). All of these measurements are consistent with each other when adjusted for technique, geometry, and scan protocol (i.e., number of projections).

II.C.6. Mega-voltage CT

Another option for on-line CT imaging is to use the MV linear accelerator as the radiation source, rather than adding a diagnostic x-ray tube. A number of research MVCT systems have been developed, of which one of the earliest to be used clinically is the system at the University of Tokyo,[46] which uses a cadmium tungstate detector for improved efficiency. It collects complete 3D images in approximately 38 s in a fan-beam scan mode at doses of 14 to 28 mGy and has a resolution of 3.5 mm. Beam energy is 6 MV. This system has been used for patient setup/repositioning and real-time beam monitoring during stereotactic radiosurgery.

An MVCT system was also developed as part of the University of Wisconsin TomoTherapy project, and has since been commercialized as part of the Hi-Art® system by TomoTherapy, Inc. (Madison, WI). This integrated system is based upon a CT gantry and can operate in both a therapeutic and MVCT imaging mode. The MVCT uses a 738 channel xenon CT detector that is approximately 20% efficient at MV energies. The scan time is currently 5 s per slice. The total imaging dose depends upon the scan protocol (e.g., pitch, slice thickness, dose rate, etc.) and the patient size, but among the 28 centers clinically treating with TomoTherapy, the typical range is between 10 and 30 mGy. This dose shows contrast of 2%–3% and resolution of 1.4 mm. (For comparison, diagnostic CT typically has spatial resolution of about 0.75–1.0 mm at high contrast and resolution of a few millimeters at 0.5% contrast.[33,47]) The scan range of the MVCT is selectable to cover as much or as little of the tumor/anatomy as necessary for setup and registration.

Cone beam MVCT has been implemented clinically at the University of California, San Francisco, in partnership with Siemens Medical,[38] and at the Memorial Sloan-Kettering Cancer Center (MSKCC), in collaboration with Varian Medical Systems. Both of these systems are based on conventional linacs. The MSKCC system can obtain an MV cone-beam CT of the thorax suitable for tumor delineation from 100 projections using a total of 20 MU of radiation.[48] Low-dose cone-beam MVCT is complicated by variations in beam flatness, symmetry, and other characteristics when the LINAC is operated at low output. In each case, continuing investigations are being made into more efficient detector technologies to reduce dose and improve image quality.

II.D. Fluoroscopy

Fluoroscopy is the most used imaging technique during image-guided surgical interventions. Its use in radiation therapy has been mainly in a similar vein, for surgical guidance assistance during brachytherapy seed insertion, but it is also entering wider use to monitor anatomical movement before and during external beam radiotherapy.

II.D.1. C-arm fluoroscopy

Fluoroscopy requires the continuous (or near-continuous) delivery of x-ray flux to obtain a real-time radiographic record of changing anatomy. Typical fluoroscopic units such as C-arms with x-ray image intensifiers will automatically adjust the kV/mA technique to obtain acceptable images. The automatic settings compensate for the total attenuation through the patient in order to maintain an adequate signal-to-noise at the image intensifier and thus will vary widely from site to site and according to the patient's weight. Furthermore, different C-arms can have different sensitivity levels, and the functioning of the individual systems can be variable due to quality control and system calibration, etc. This results in a spread of dose levels for any particular exam.

There have been numerous surveys of typical or routine exposure levels for C-arm fluoroscopy that include ranges around the mean exposure level. The 2002 Nationwide Evaluation of X-ray Trends (NEXT) survey of x-ray exams reported a median entrance dose rate (EER) of 22 ± 14 mGy/min for mobile C-arm units imaging a phantom equivalent to 21.5 cm of water 30 cm above the image intensifier [USFDA Nationwide Evaluation of X-ray Trends (NEXT)[49]]. This would be the average dose rate for an abdominal fluoroscopic exam, with somewhat less dose for a thoracic exam. Therefore, for pretreatment fluoroscopic studies of thoracic and abdominal organ motion the typical entrance dose to the patient will be (within a factor of 2) approximately 20 mGy/min.

The typical source-detector distance for a C-arm is approximately 100 cm. With an adult patient in the field of view this creates a tight geometry in which the entrance skin dose can change dramatically if any part of the patient moves closer to or further from the source. Moving the C-arm by only a small amount during the procedure can risk serious skin injury. One must therefore be alert to the position of the patient at all times during the imaging procedure.

II.D.2. Varian on-board imager (OBI) and Elekta synergy XVI

Both the Varian OBI and Elekta XVI CBCT systems can operate in fluoroscopic mode. The Elekta system has a source/isocenter distance of 100 cm and a combination of 2 mm Al and 0.1 mm Cu filtration at the tube. Islam *et al.*[42] have measured the dose rate delivered by the Elekta system in fluoroscopic mode to be 0.06 mGy/mAs at 100 kVp and 0.1 mGy/mAs at 120 kVp. This is the dose at the surface of a 16 cm diameter cylindrical head phantom. For a technique of 100 kVp, 25 mA, and 4 ms exposure per frame[50] this would correspond to a fluoroscopic dose rate of 10.8 mGy/min. This is about $\frac{1}{2}$ the dose rate of a typical C-arm (see Sec. II D 1) and a little more than the entrance skin dose rate measured for the Hokkaido fluoroscopic system (see Sec. II D 3 and Table I). (However, if the Hokkaido system were to be run at the same equivalent technique for the $1/r^2$ difference in geometries, it would deliver about 1.8 times as much dose.)

II.D.3. Dedicated in-room fluoroscopy

A technique of dual-view fluoroscopy for tumor tracking during radiotherapy has been developed at the Hokkaido University School of Medicine. The imaging system consists of four diagnostic x-ray sources and four x-ray image intensifier units configured around the treatment isocenter as shown in Fig. 5. The rectangular x-ray field at the patient is 14 cm $\times$ 19 cm. The source/isocenter distance is 280 cm, and the isocenter/detector distance is 180 cm.[11] During each treatment fraction, two of the four imaging systems are used to locate and continuously track radio-opaque artificial fiducials implanted at the treatment site.[51] The image data from the two views are combined to obtain precise 3D trajectories of the treatment site.[52,53] A particular pair of imaging systems can be selected to avoid interference by the gantry and LINAC in the imaging lines of sight. Each imaging system acquires 30 frames per second using a nominal exposure time of either 2 or 4 ms per frame. The exposure level and detector sensitivity are sufficient to observe fiducial markers in the lung, in the liver, and in the pelvis.[54,55]

Table III summarizes the air kerma measured at the isocenter for each of the imaging techniques used during treatment.[56] For lung and liver tracking the technique uses 80–125 kV, 80 mA, and either 2 or 4 ms exposure duration per frame. (These are nominal exposure times—high-voltage x-ray tubes do not switch on and off instantaneously.) Because the patient's skin surface is typically closer to the source, resulting in a higher dose, the data of Table I have also been scaled by $1/r^2$ to estimate the entrance skin dose when the patient's skin surface is displaced by 5 cm, or 30 cm, from the isocenter towards the source. Treatment is always done with two diagnostic beam viewpoints, so wherever the two imaging beams overlap the total skin dose is twice the dose in Table III.

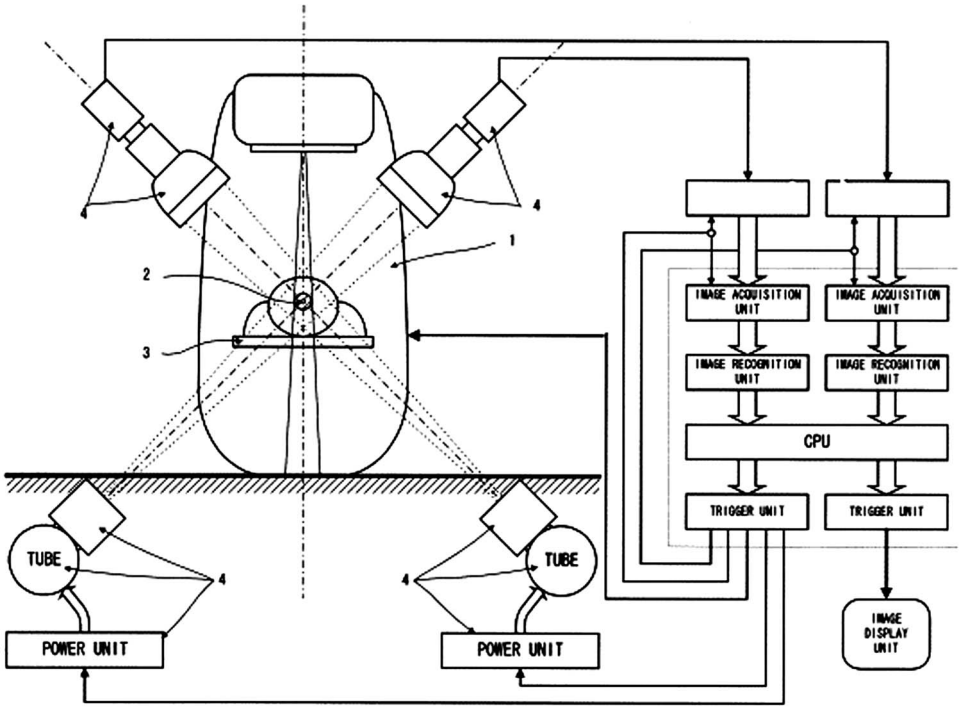

FIG. 5. Fluoroscopic tracking system at Hokkaido University.

III. IMAGING SCENARIOS FOR IGRT

III.A. Planning

Because of the special utility of the CT Hounsfield number in treatment planning, x-ray CT will remain the primary imaging modality for radiotherapy planning for the foreseeable future. Conventional planning requires one axial or spiral CT assuming a motionless patient. When imaging treatment sites that move during breathing, motion artifacts can be reduced using respiration-correlated CT. This procedure involves acquiring an oversampled CT data set that is time stamped so that the data can be sorted into time bins corresponding to discrete moments of the breathing cycle (see Sec. II C 3).

Cone-beam CT is currently under development and can potentially be used for pretreatment planning (as with the Varian Acuity system). However, it is subject to cupping artifacts and inaccuracies in the Hounsfield number due to its significantly higher scatter-to-primary-fluence ratio.[57] These inaccuracies can affect the accuracy of the electron densities that are used for dose calculation. Charge trapping and incomplete readout in the solid-state imaging panel (image lag) can also make it susceptible to streaking and blurring artifacts that do not arise in fan-beam CT.[57] Consequently the primary use at present is for in-room setup (see Sec. III E 3).

Megavoltage CT has less contrast than kV CT but it also has less streaking artifact due to high-Z materials. Furthermore the reconstructed Hounsfield numbers more closely represent the attenuating electron densities seen by the treatment beam, making it useful to the dose calculation component of the treatment planning process.

TABLE III. Entrance air kerma at the patient from the Hokkaido fluoroscopic tracking system for an exposure period of 60 s at 30 image frames per second.

			Air kerma @ Patient (mGy)		
kV	mA	ms	@Isocenter	5 cm from Isocenter	30 cm from Isocenter
60	80	2	1.11	1.14	1.38
		4	2.07	2.15	2.60
80	80	2	2.45	2.54	3.07
		4	4.28	4.44	5.37
100	80	2	4.35	4.51	5.46
		4	7.41	7.68	9.30
120	80	2	6.69	6.94	8.39
		4	10.90	11.30	13.67

III.B. Pretreatment fluoroscopy for motion estimation

Modern techniques to deal with intrafraction organ motion due to respiration are aimed at managing the motion rather than accommodating it via large planning margins. There are three basic approaches to the management problem: (1) reduction of the motion via breathholding,[58–61] active breathing control,[62] or assisted ventilation;[63] (2) temporal tracking by detecting the breathing phase and gating the beam on and off synchronously with the breathing cycled;[64] (3) spatial tracking by detecting the tumor position and shifting the alignment of the beam synchronously.[65] All three techniques require a pretreatment assessment of the motion to define parameters for its management. Respiration-correlated 4D CT provides one means to analyze the motion over a short time interval (e.g., a few breathing cycles), but the motion is sufficiently complex that longer periods of ob-

servation are frequently necessary. This can be accomplished with fluoroscopic imaging for periods ranging from 30 s to several minutes.[2] The imaging dose delivered during a 5 min fluoroscopic study can exceed 100 mGy and must be included in the overall imaging dose budget for the patient.

III.C. Brachytherapy guidance

Diagnostic imaging to support brachytherapy can involve CT, film-based radiography, C-arm fluoroscopy operated in continuous or single-frame mode, and simulators.[66] There are a number of different diagnostic imaging scenarios to support brachytherapy, depending on the procedure. There is also considerable variability among different institutions. For example, tandem and ovoid procedures involve either a whole-pelvis CT or orthogonal films for each fraction. Most practitioners in LDR for prostate implants use fluoroscopy (continuous or single-frame mode) during the procedure and a followup CT after the implant (in some institutions on day 1; in other institutions on day 30). In prostate HDR fluoroscopy is again used during the catheter implantation; this is repeated for fractionated treatments. If prostate HDR is combined with external-beam radiotherapy, a CT study will also be acquired. Endometrial and cervical HDR include films for every fraction. The MammoSite procedure is typically guided by an evaluation CT, multiple CTs during placement, and films for each fraction, although some institutions have replaced the films with ultrasonography.

III.D. Simulation

Simulation refers to the acquisition of reference setup images to which the in-room setup images are compared to determine how close the target is to the planned position. Historically these images were acquired after the CT study in a separate pretreatment procedure using a kV imaging system that approximately reproduced the patient's position in the planning CT. This therefore added one or two planar diagnostic-quality kV images to the total imaging budget. For a film-screen-simulation system, and assuming 400 film speed and 125 kVp, the typical chest simulation would require 0.025 mSv for AP and 0.075 mVs for lateral.[33]

With the advent of fast beam's-eye-view DRR computation the reference images can now be obtained directly from the planning CT (virtual or CT simulation), thus eliminating the additional imaging dose while improving the accuracy of the patient setup process. This advance in image-guided radiotherapy is one of the rare instances in which the imaging dose has been reduced while increasing the treatment accuracy.

III.E. Interfraction setup

After CT-based planning, the most common use of imaging during radiotherapy is patient setup at the beginning of the fraction. This was initially done with megavoltage portal imaging but now can also be done with in-room planar kV imaging, or in-room CT. For 3D setup it requires one or more pairs of orthogonal images.

III.E.1. Portal

Several types of fractionated schedules are followed for portal imaging.[67] The most conservative is weekly acquisition of images, which is appropriate for treatment plans that are not highly conformal. More precise targeting is enabled by taking portal images daily for a week to assess tumor position variability and systematic setup error, followed by weekly imaging after correction for systematic offsets. Highly conformal techniques can call for daily imaging.[68] The advent of solid-state portal detector systems, which are more efficient than film systems and thus require less dose, has encouraged more frequent imaging schedules.

For each schedule there are several imaging scenarios. The crudest is a single AP image for 2D positioning. Three-dimensional positioning requires two images, which by convention are anterior/posterior (AP) and lateral. These viewpoints were inherited from diagnostic imaging conventions and are not optimal for 3D position estimation—the AP image quality is always much better than the lateral quality. Two oblique viewpoints can provide better position reconstruction (cf. Figs. 1, 2, and 5). As Table IX in Sec. IV A 3 shows, the effective dose from the exposure depends on viewpoint. Some setup procedures involve a double exposure technique for each viewpoint. Finally, highly conformal treatments sometimes include a second set of portal images at the end of the fraction to fully document the patient's position. Therefore the most meticulous and conformal setup procedure could involve daily dual-view double exposures followed by end-of-fraction verification imaging. This adds up to 180 portal images for a thirty-fraction treatment.

III.E.2. In-room kV radiography

In-room kV imaging systems replace the function of the EPID for setup based on dense radiographic landmarks such as bone and implanted fiducials. It almost always involves taking dual orthogonal images at either traditional AP/lateral viewpoints or oblique angles (cf. Figs. 1, 2, and 5). The setup procedure can involve one, two, or more pairs of images, depending on the criteria for targeting precision. For highly precise targeting, as required by radiosurgery for example, the first image pair indicates a coarse setup correction, followed by a second image pair to verify and/or provide a further fine position correction, sometimes followed by another image pair to verify final positioning. The gantry-mounted Varian OBI can be used in this capacity.[28]

III.E.3. In-room CT

In-room planar radiography is useful for setup guided by either bony landmarks or implanted fiducials but is of limited use in assessing soft tissue position and shape. In-room CT has been developed to assist soft-tissue target alignment before the start of treatment.[69] In one approach a conventional CT scanner is placed in the treatment room on the same couch axis as the LINAC gantry. A single couch serves the CT scanner and the beam delivery system (see CT-on-rails, Sec. II C 4). Another approach uses a kV source and diagnostic detector mounted to the treatment gantry at 90° with

respect to the LINAC. The gantry is rotated to obtain a kilovoltage cone-beam CT. A third approach uses the treatment beam and a gantry-mounted EPID to obtain a megavoltage cone-beam CT. TomoTherapy uses an MV linac rotating in a CT-like gantry to obtain megavoltage CT in a fan-beam scan mode.

Regardless of how in-room CT images are collected, the most common application for them at present is patient setup verification and repositioning. In this process, the imaging system is used to collect a CT volume of the patient immediately prior to treatment. While most systems have the technical ability to offer improved image quality at higher doses, or noisier images at lower doses, it is nonetheless common at present for most to maintain $CTDI_w$ (or its cone-beam counterpart) in the 10–50 mGy range. Once the images are collected, tools are usually provided for manual or automatic image registration, and an ability to conveniently reposition either the patient or therapy beam in the treatment room. Beyond registration and repositioning, there are numerous more advanced applications for in-room CT images. These concepts are broadly categorized as adaptive therapy or the use of feedback in improving patient treatments. Examples of adaptive therapy include modifying contours or plans to account for anatomical changes, dose reconstruction, and image/dose deformation.

III.F. Intrafraction monitoring

Intrafraction imaging is important for situations where the target can move significantly or where the precision requirements are strict enough to warrant constant surveillance of the target during irradiation (e.g., frameless radiosurgery). The image data can be used as a passive record of target position, or to gate the beam, or to adjust the beam alignment with the target. However, to use the image data to actively maintain beam alignment, it must be possible to realign the beam with the patient automatically during treatment (by moving either the linac or the patient). Presently, the CyberKnife is the only commercial radiotherapy system with this capability.

III.F.1. kV Radiography

The BrainLab ExacTrac system is capable in principle of acquiring radiographs during the treatment fraction (both between and during beams) although scatter from the treatment beam into the kV imaging panels will degrade image quality, and presently there is no capability to automatically realign the patient in response to changes in target position. Likewise, the Varian OBI and Elekta systems could in principle provide intrafraction radiography, although their gantry mounting restricts them to a single 2D viewpoint at a time and requires a more sophisticated technique for image registration as the imaging viewpoint moves during treatment.

The CyberKnife imaging system is presently the only commercial system used for initial patient positioning followed by periodic position remeasurement during the fraction. After each new measurement a robotic manipulator moves the beam to the newly detected target position. The treatment regimen is either single-fraction radiosurgery or hypofractionated radiotherapy (2–5 fractions). Typical imaging frequency is 30–50 image pairs per fraction (1–2 acquisitions per minute) but it can be increased to provide images every few seconds or decreased to provide only setup and position verification data. The imaging duty cycle for any particular patient is usually adapted to the frequency and magnitude of patient movement detected during treatment.

In typical cranial radiosurgical treatments, the entire treatment dose is delivered in one fraction while approximately 30 image pairs are taken at 30–60 s intervals to track target position.[70] This results in a total entrance dose in air of 7.5 mGy. Spine treatments are typically divided into three fractions with 20–40 image pair acquisitions per fraction,[70] for a total average entrance dose in air ranging from a minimum of 22.5 mGy for the C-spine to a maximum of 200 mGy for the sacrum.

III.F.2. kV Fluoroscopy

Fluoroscopic monitoring of the treatment site is being used at Hokkaido University to gate the therapy beam.[11] The prototype Hokkaido system operates in pulsed fluoroscopic mode, acquiring 30 frames per second with either 2 or 4 ms exposures. Images are acquired continuously during the treatment irradiation. To reduce the amount of dose from fluoroscopy, the pulse rate is changeable from 30 to 15, 10, 5, and 2 frames in the second-generation system.[71] The position of the patient couch can be adjusted using an on-line remote control unit at the console of the LINAC outside of the treatment room. Ten systems in eight hospitals are actively used in Japan but the machine is not commercially available at present.

III.F.3. MV-EPID cine mode imaging

It is possible to acquire portal images continually during the fraction for passive monitoring of patient position. In this mode the EPID images are acquired continuously without a trigger from the linac. For example, the Varian AS500 EPID (Varian Medical Systems) is capable of operating in *cine* mode at approximately one frame every 1.6 s. This imaging mode has the distinction of being the only approach that uses the actual therapy radiation (rather than an open field) and thus adds no extra dose.

IV. DOSE EVALUATION

The AAPM Task Group on Reference Values for Diagnostic Radiography takes the position that clinicians should not be held to strictly defined limits on radiographic exposure to patients but should be aware that, when their exams significantly exceed a typical or reference dose level as represented by an agreed upon "reference value" for that category of exam, the clinician should take steps to reduce the exposure levels.[24]

The data tabulated for all of the imaging procedures used in image-guided radiotherapy show that a typical image-guided treatment scenario involving a 4D CT and intrafraction motion tracking will involve doses that are 10 to 100

times the reference values for diagnostic imaging of the same part of the anatomy.[24] This underscores the fact that IGRT presents an entirely different situation in radiographic exposure and that the diagnostic reference values are not relevant. The IGRT imaging dose can be divided into four categories: (1) kilovoltage skin dose, (2) kilovoltage organ dose, (3) megavoltage skin, and (4) megavoltage organ dose.

The U.S. Food and Drug Administration has issued an advisory on the skin injury risks associated with complex image-guided interventional procedures that can involve long exposures to fluoroscopy and other diagnostic imaging x-ray procedures. The National Cancer Institute has also recently published an advisory on the risks associated with interventional fluoroscopy.[72] These advisories note the following approximate threshold dose levels at which eye and skin injuries of increasing severity can occur,[12,72] based on evidence accumulated following a variety of fluoroscopically guided interventions:

Effects	Threshold	Time of Onset
Early transient erythema	2000 mGy	2–24 h
Temporary epilation	3000 mGy	1.5 weeks
Main erythema	6000 mGy	3 weeks
Permanent epilation	7000 mGy	3 weeks
Dermal necrosis	15,000 mGy	>52 weeks
Eye lens opacity (detectable)	>1000 mGy	>5 years
Cataract (debilitating)	>5000 mGy	>5 years

These observations are based on a wide range of imaging scenarios, including procedures performed in one long session and procedures repeated many times over several weeks, making it difficult to establish the significance of the time period over which the dose is delivered. By way of comparison, an IGRT treatment involving a 4D planning CT, 5 min of pretreatment fluoroscopy to assess tumor motion, followed by thirty fractions of fluoroscopically guided radiation therapy (2 min per fraction), ending with a follow-up CT can result in a total skin dose exceeding 1500 mGy. Daily CT for patient setup can add 1000 mGy of both skin and organ dose. Although the imaging dose in interventional fluoroscopy is typically delivered over a much more compressed time scale than in conventional IGRT, which might be a factor influencing the injury thresholds, it should be recognized that in the most aggressive applications of IGRT the concomitant imaging exposure can approach levels at which deterministic injury might be a potential outcome.

Imaging dose during radiotherapy is often discussed in relation to the total therapeutic dose to the target and/or the concomitant background and scatter dose from the beam, expressed in cGy. This direct comparison is inappropriate and misleading because of the varying biological effects associated with different dose delivery scenarios. To provide an approximate basis for comparison of imaging dose to therapy dose we must convert all the doses to a common unit of radiobiological effect—namely the effective dose. The conversion process depends on how the radiation is distributed through the anatomy, how it deposits energy locally, and how the deposited energy affects biological entities. There are established procedures for converting different imaging doses to effective dose, but, as mentioned earlier, little has been done to study the conversion of therapeutic dose into effective dose. The main difficulty in analyzing effective therapeutic dose is the fact that, while imaging procedures tend to follow standardized scenarios, therapeutic irradiation is patient specific. Furthermore, Aird[1] points out that the special health characteristics of the patient subgroup undergoing therapy will bias the evaluation of biological effect underlying the concept of effective dose. (We note, however, that this same circumstance can also bias the calculation of effective diagnostic imaging doses.) Therefore this report is limited to a discussion of how to compile diverse imaging doses into a total effective imaging dose.

IV.A. Conversion of imaging dose to effective dose

The only dose quantity that allows any intercomparison of stochastic risk between the different imaging scenarios described in this report is effective dose, which combines the quality and distribution of radiation throughout the body with its effect on a number of specific organs. It is distinguished from equivalent dose, which is a local measure of biological effect obtained by multiplying local absorbed dose at a point in a specific organ by a biological weighting factor. Effective dose is computed by weighting the equivalent dose values for various organs by the organ weighting factors and then summing over the exposed volume so as to obtain an equivalent whole-body dose. It is therefore actually an expression of integral dose rather than local dose deposition. The precise effective dose depends on the imaging modality, the energy of the radiation, the age and sex of the patient, and the anatomical particulars of the exam. The effective dose is obtained from the absorbed dose D (mGy) via a semiempirical conversion factor F (mSv per mGy) such that

$$E = D \cdot F[mSv/mGy]. \tag{3a}$$

The quality factor F has been tabulated for different exam types. It can be expressed in terms of dose-to-air (i.e., absorbed dose measured with an ionization chamber in a phantom, with scatter included) or dose-free-in-air (i.e., dose-to-air without a phantom and thus with no scatter). This distinction is important when analyzing CT doses.

Converting the megavoltage x-ray dose from portal imaging, expressed in MU or cGy, into effective dose presents some special difficulties that make the conversion more difficult than for diagnostic imaging. These difficulties include the difference between air kerma and absorbed dose in regions of nonequilibrium (such as the skin and air/organ interfaces) and the differences in dose intensity and gradient noted in Sec. I D. Nevertheless, it is possible to make some useful approximate evaluations of megavoltage imaging dose for general comparison to diagnostic imaging dose.

IV.A.1. kV Planar imaging

The effective dose for planar projection radiography is most directly obtained from the dose-area product (entrance

TABLE IV. Conversion coefficients to give effective dose (mSv) from dose-area product of entrance skin dose (mGy cm^2) for AP projections. The total filtration is in millimeters of aluminum. All conversion coefficients are mSv/mGy cm$^2 \times 10^{-5}$.

kVp	Filter (mm Al)	Head (10^{-5})	Chest (10^{-5})	Lumbar Spine (10^{-5})	Abdomen (10^{-5})	Pelvis (10^{-5})
80	2	3.0	21.5	18.9	16.8	20.0
	4	4.1	26.9	24.9	22.2	25.2
100	2	4.1	25.5	24.0	21.5	24.3
	4	5.3	31.0	30.2	27.2	29.6
120	2	4.9	28.9	28.0	25.2	27.7
	4	6.1	33.9	33.8	30.5	32.6

skin dose in mGy times the exposed area). Le Heron[73] has computed a table of conversion factors for AP and lateral radiographs of different anatomical sites as a function of x-ray energy spectrum, organized by tube voltage and filtration thickness. A subset of these conversion factors is presented in Tables IV and V.

As an example, we calculate the conversion factor from entrance dose (mGy) to effective dose (mSv) for AP projections of the chest using a circularly collimated field 25 cm in diameter at the patient. For 80 kVp and 2 mm of filtration, we multiply 21.5×10^{-5} mSv/mGy cm^2 by the 491 cm^2 area of the exposed surface of the patient to get the conversion coefficient of 0.11 mSv/mGy.

IV.A.2. kV Fan-beam CT

Because CT, unlike planar radiography, delivers a uniform amount of radiation throughout the imaged volume, its biological impact on individual organs differs significantly from the dose from planar imaging. Furthermore, the internal dose from CT is orders of magnitude higher than for planar radiography. Therefore to make a meaningful comparison between planar and CT dose, one must convert $CTDI_{air}$ to effective dose. This conversion must account for variations in biological effect to different organs and additional factors to accommodate scan length, beam quality, etc. All of these effects combine into a conversion factor F (mSv/mGy) to give an effective dose for comparison to other radiographic procedures:

TABLE V. Conversion coefficients to give effective dose (mSv) from dose-area product of entrance skin dose (mGy cm^2) for lateral projections. The total filtration is in millimeters of aluminum. Conversion coefficients are mSv/mGy cm$^2 \times 10^{-5}$.

kVp	Filter (mm Al)	Head (10^{-5})	Chest (10^{-5})	Lumbar Spine (10^{-5})
80	2	2.9	8.3	8.1
	4	4.0	10.9	11.0
100	2	3.9	10.6	11.0
	4	5.0	13.3	14.2
120	2	4.7	12.5	13.5
	4	5.8	15.0	16.7

TABLE VI. Typical values of the conversion factor F from $CTDI_{air}$ (in mGy) to effective dose E (in mSv) for adult patients for recent routine CT exams in Germany (Ref. 74).

Examination	Scan Length (cm)	Pitch	Factor F	$CTDI_{air}$ (mGy)	E (mSv)
Head	12.0	1.0	0.023	81	1.9
C-spine	18.0	1.2	0.044	55	2.4
Chest	27.0	1.3	0.136	47	6.4
Abdomen	42.0	1.3	0.239	54	12.9
L-spine	6.0	1.1	0.029	100	2.9
Pelvis (male)	24	1.2	0.137	60	8.2

$$E = \mathrm{CTDI}_{\mathrm{air}} \cdot F[\mathrm{mSv/mGy}]. \quad (3b)$$

A detailed evaluation of the overall conversion factor F depends on the scan length and is therefore developed by summing contributions along the length of the scan using a factor $f(z)$ per 1 cm of slice thickness. Examples of the conversion factor per unit length $f(z)$ and the composite conversion factor F for different patient characteristics and organs can be found in Nagel.[33] Table VI summarizes typical doses in air, effective dose conversion factors, and effective doses for several exam types.

Table VII was generated using data collected all over Europe for dual and multiple CT scanners. It is an excerpt of data for the years 2000 and 2002 from the original table published by Friberg.[75]

IV.A.3. kV Cone-beam CT

Endo *et al.*[45] have made dosimetry measurements for a kilovoltage cone-beam CT system that utilized a 45 cm $\times$ 60 cm fluorescent screen coupled to a lensed CCD image intensifier. The imaging plane was oriented such that its long axis was parallel to the patient's cranial/caudal axis. They measured mean and maximum entrance skin dose as well as organ dose, from which they calculated effective doses for a head and a chest exam. The results are summarized in Table VIII. The effective dose conversion factor (effective dose divided by mean skin dose, divided by detector area) of 6×10^{-5} mSv/mGy cm^2 for cone-beam head exams is about 25% greater than the factor for planar diagnostic head exams (Tables IV and V). The cone-beam conversion factor for a chest exam is about 25% less than for planar diagnostic imaging. When compared to fan-beam CT, the cone-beam con-

TABLE VII. Mean Values of the effective dose (E), $CTDI_{vol}$, and DLP (Ref. 75).

Examination	Period (yr)	E (min–max) (mSv)	$CTDI_{vol}$ (min–max) (mGy)	DLP (min–max) (mGy cm)
Head	2002	2.2 (1.3–3.7)	79 (45–116)	991 (590–1626)
Chest	2002	5.8 (1.8–11.3)	10 (4–17)	317 (102–647)
Abdomen	2002	11.4 (7.4–14.7)	12 (8–19)	643 (389–847)
LS	2000	4.3 (2.3–9.3)	34 (19–54)	265 (165–396)

TABLE VIII. Dose from kV cone-beam CT (Ref. 45).

Parameter	Head	Chest
Maximum skin dose (mGy)	100.5	85.4
Mean skin dose (mGy)	68.5	57.0
Effective dose (mSv)	10.9	24.6
Conversion factor (mSv/mGy cm^2)	6.0×10^{-5}	16.0×10^{-5}

version factor is about the same for the chest and about 40% higher for the head, when corrected for scan length and axial pitch.

The measurements by Islam *et al.*[42] for the Elekta kV cone-beam system are given in Table IX. Note that because the detector's longitudinal dimension is less than the system measured by Endo,[45] the DLP and consequently the effective dose are less as well.

IV.A.4. Portal imaging

The dose from portal imaging contributes direct dose to the target volume and concomitant exposure elsewhere, with an additional component of direct dose outside the target cross section due to the uncollimated/unblocked field of exposure. The direct target dose should be included in the planned therapeutic dose. Waddington and MacKenzie[68] have made an approximate conversion of portal imaging dose to effective dose for various treatment sites. This evaluation is based on the anatomy of an adult of average height and weight. Because effective dose is calculated from the distribution of radiation among organs of variable risk, it will vary from patient to patient, but the average scenario presented here should suffice for a factor of 2 level of accuracy. Table X summarizes the results of Waddington and MacKenzie for a 6 MV extended field (18 cm$\times$15.6 cm) at an SSD=88 cm.

IV.A.5. MV cone-beam imaging

MV cone-beam imaging is practiced only at a small and select number of facilities. We are unaware of any systematic evaluation of its effective dose. However, MV radiation has a relatively small attenuation gradient through the anatomy, in contrast to the steep gradient for diagnostic energy radiation. Therefore we assume that, to a first approximation, the effective dose for MV cone-beam imaging can be estimated by summing the individual doses from each gantry angle using for each projection the portal imaging conversion factor of Table X for the examination site. (There has not been a published report on effective dose calculated directly for MV cone-beam CT, so the assumption here is that the field of view for a single projection in MV CBCT is comparable to an open-field portal image.) Because of the difference between AP and lateral doses, the summation should be an AP/lateral average weighted by the angular position of each image acquisition.

TABLE IX. Dose from the Elekta XVI kV cone-beam CT (Ref. 42).

Parameter	Head	Chest
Mean dose at center (mGy)	29	16
Mean skin dose (mGy)	30	23
Effective dose (mSv)	3.0	8.1
Conversion factor (mSv/mGy cm^2)	6.0×10^{-5}	16.0×10^{-5}

TABLE X. Effective dose E from 6 MV portal images 18 cm$\times$15.6 cm taken at SSD=88 cm (Ref. 68).

Port View	Gender	Effective Dose E (mSv/MU)
AP pelvis	Male	0.34
	Female	0.52
Lat pelvis	Male	0.32
	Female	0.7
AP chest	Male	1.74
	Female	1.8
Lat chest	Male	2.56
	Female	2.23
Lat neck	N.A.	0.12

IV.B. Examples of cumulative imaging dose and stochastic risk

The most recent ICRP coefficient for estimating the lifetime probability of inducing a fatal cancer from a single radiographic exposure is 5×10^{-5} per mSv of effective dose.[76] This coefficient is based on the linear no-threshold model of radiation risk and is derived primarily from studies of atomic bomb survivors. For image-guided radiotherapy the estimate is overly simplistic, as it neglects details such as the time period over which the dose is delivered, as well as the age and sex of the patient, i.e., how does one handle the difference between a single CT and a sequence of portal images taken over many days? Nevertheless it provides a starting point to evaluate the added risk from imaging exposures during radiotherapy. We use this simple estimate in the following examples of image-guided radiotherapy scenarios.

Consider a prostate treatment routine that involves a conventional fan-beam CT for planning (60 mGy, 8.2 mSv, from Table VI) followed by 30 daily portal image pairs at 2 MU each (30$\times$1.3 mSv, from Table X). This delivers a total effective imaging dose of 47.2 mSv. Using the ICRP-60[76] coefficient of 5×10^{-5} there is an estimated probability of 0.2% of radiation-induced cancer in the patient's lifetime. For a 70 year old this might be considered an inconsequential risk.

As a second example, consider a 30 year old female being treated for cervical cancer. If that patient undergoes 30 complete daily in-room CTs for targeting and compensation of organ deformation (30$\times$8.2 mSv, from Table VI), she receives an estimated 246 mSv of effective dose, resulting in a 1.2% probability of a radiation-induced cancer. However, we note from Table X that the female pelvis is more radiation sensitive than the male pelvis (where the gonads can be shielded), so this risk estimate is likely to be low.

Although it is difficult to know how to evaluate added cancer risk in patients that already have cancer, it remains true that some of the added risk is negotiable, in the sense that added imaging can improve the therapeutic ratio for the primary disease. The risk/benefit trade becomes more complex when one considers that many radiotherapy procedures address noncancerous diseases. For example, radiosurgery is commonly used to treat arteriovenous malformations (AVMs),[77,78] acoustic neuromas,[79] trigeminal neuralgia,[80] and pituitary adenoma.[81–83] The advent of frameless image-guided radiosurgery adds imaging dose to the concomitant dose from the therapy beam, increasing the risk of inducing a primary cancer.

For a third case we use the Hokkaido Hospital fluoroscopy system described in Sec. II D 3 to image continuously for 2 min per fraction, over 30 fractions. The treatment site is the lung, the technique is 100 kVp, 80 mA and 4 ms pulsed exposure. The inherent x-ray filtration is 3.5 mm aluminum equivalent.[71] The exposure area for each imaging view is 266 cm^2, for a total of 532 cm^2. From Table II one finds the dose-in-air per minute at the isocenter is 14.82 mGy. From Tables IV and V for effective dose from planar radiographs we average the AP and lateral factors to account for the oblique imaging angle in Fig. 1, giving a total effective dose of 1.75 mSv per fraction, or 52 mSv over the course of treatment. With the addition of a treatment planning CT the patient receives a total of 60 mSv of imaging dose, corresponding to a 0.3% additional risk of radiation-induced cancer.

IV.C. Comparison of imaging dose to concomitant dose from the therapy beam

At some point an evaluation of imaging dose in IGRT must involve comparisons to primary and secondary (concomitant) dose from the treatment beam. We have already indicated that this is a nontrivial problem for two reasons: (1) therapy dose distributions are far more individualized than imaging doses, and (2) the estimation of effective dose from the therapy beam has rarely been attempted. Therefore the task group did not undertake to study the problem of concomitant therapy dose or to compare imaging dose to primary and secondary therapy dose. However, we provide here some examples of secondary therapy dose estimations to provide the practitioner with some direction in making case-by-case clinical evaluations.

Secondary treatment dose has two principal components: (1) An external component from collimator leakage, scatter from materials outside of the patient, etc. and (2) an internal component from interactions of the primary therapy beam with the patient.

In a phantom/simulation study, Diallo *et al.*[84] developed a computational program to estimate total internal and external scattered dose to anatomy outside the target volume for a comprehensive range of treatment variables. By entering patient-specific parameters such as treatment site, patient height and weight, and treatment beam characteristics, etc., the user obtains a map of concomitant dose elsewhere in the body. In two examples, a 60 Gy breast treatment delivered 220 mGy of secondary dose to the lower thorax, while a 60 Gy head/neck treatment to a target near the base of the skull delivered 240 mGy to the pectoral region of the chest. As one would expect, the secondary dose falls off rapidly with distance from the treatment site, making it difficult to summarize or compare to distributions of imaging dose.

In a clinical case study of one example prostate IMRT treatment, Cigna *et al.*[85] measured the total scattered dose from both internal and external (a 6 MV Varian Clinac 6/100) sources using ten pen dosimeters arranged at various points on the surface of the patient's body. Again, the geometrical distribution of scattered dose fell off steeply with distance from the target (e.g., by a factor of approximately 25 in the first 10 cm away from the isocenter). From their measurements the authors calculated a total secondary effective dose of 854 mSv produced by a total primary target dose of 70.2 Gy. The presentation of the results in terms of effective dose properly accounts for both the geometric dose distribution and differing radiosensitivity within the anatomy. It is important to note that more than $\frac{3}{4}$ of the effective dose for this particular treatment scenario was due to exposure of the testes, which are close to the target and have a high radiosensitivity.

We also take note of a Monte Carlo simulation of internally scattered secondary radiation in a phantom, by Ing *et al.*,[86] who report their results in total integrated dose (gram - mGy) over the entire phantom volume. This study does not allow direct comparison to the other two estimates cited here, as the integration in cGy over volume washes out the falloff with distance from the target without making the conversion to integral effective dose.

Perhaps the most significant point to be made by these examples is that the secondary therapy dose is dominated by internal scatter, which depends on many clinical parameters (beam energy spectrum, geometry of fields, position of treatment site, patient shape and size, IMRT versus 3D versus conventional) that vary significantly from one patient to the next. While it is feasible to collect imaging doses from standardized imaging techniques into a report such as this, it may never be feasible to summarize concomitant therapy dose in a comparable way.

V. DOSE REDUCTION AND OPTIMIZATION

The general rule adopted for dose management in diagnostic imaging is represented by the acronym ALARA—as low as reasonably achievable. For imaging associated with radiotherapy we will address methods to reduce the effective dose without reducing the image information, e.g., by narrowing fields of view, using more efficient imaging modes and techniques, etc.

In diagnostic imaging there is a direct relationship between exposure level and image quality. The demand for high contrast, low-noise images pushes the exposure levels up. In IGRT, the beam alignment information derived from images used for the targeting of tumors is less dependent on image quality and more dependent on imaging frequency. In each general treatment scenario, an increase in the number of

images will yield smaller errors in dose alignment, but with diminishing significance. At some point, further increases in the number of images will add more imaging radiation dose to healthy tissue than is eliminated by improved therapy dose alignment. One would like to identify this point of optimal balance between imaging dose and alignment error.

V.A. Field collimation

The U.S. Federal regulations for limiting exposure in diagnostic x-ray imaging require only that the field of view illuminated by the source not exceed the area of the sensor, since imaging exposure outside the imaging active area is obviously of no use. This is a necessary but not sufficient guideline for the reduction of unnecessary exposure. In fact, in image-guided setup and tracking all exposed volume outside the anatomy actually used to align patient and beam receives unnecessary dose that contributes nothing to the image guidance process. For a treatment in which a small cluster of fiducials within the tumor serves for beam alignment, the relevant targeting cross section can be as small as 5 cm in diameter (20 cm^2), while a 9 in. x-ray image intensifier or a 20×20 cm amorphous silicon panel has approximately 400 cm^2 of active area.

Effective dose is inherently an integral measure of dose, involving field area for planar radiography and scan length for tomography. Effective dose can be reduced by employing adjustable collimators that can limit the radiation field to the immediate vicinity of the target anatomy. This has been implemented in, e.g., the CyberKnife and the BrainLab Novalis x-ray alignment systems. Likewise, for in-room CT verification, it is recommended that one scan only as much anatomy as necessary for the desired imaging task, such as positioning a particular region of anatomy. This can be achieved easily by limiting the axial length of the scan in a slice-based scanner such as CT-on-rails or TomoTherapy, or by reducing the cone angle in the axial direction in cone-beam CT. It can also be achieved in both axial and cone-beam CT by restricting the field of view in the slice direction by collimating down the fan angle to the volume of interest,[87,88] but the resulting truncation of the projection data produces artifacts from filtered backprojection, necessitating a more sophisticated reconstruction process. Therefore reduction of the effective dose for CT by reducing the exposed volume is a more difficult process than for planar radiography. Nevertheless, a significant reduction (factor of 10) of effective dose in megavoltage CT has been achieved by reducing the fan angle without loss of image quality.[87]

V.B. Pulsed fluoroscopy

Standard fluoroscopy acquires images at the standard video rate of approximately 15 or 30 frames per second. The exposure level is set to give an acceptable image of the anatomy in each frame. Fluoroscopy in IGRT is frequently used to monitor the motion of target sites that move due to respiration and heartbeat, often using implanted fiducials to mark the target. Fluoroscopic exposure can be reduced by three means: (1) Reduction of the exposure period while maintaining the conventional rate of 30 frames per second; (2) reduction of the frame rate while maintaining the conventional exposure period of 32 ms; or (3) reduction of both the frame rate and the exposure period. At Hokkaido University the prototype fluoroscopic tracking system takes 30 frames per second of either 2 or 4 ms duration.[11] Normal respiration occurs at a frequency of 0.3–1 cycles per second while normal heartbeat is below 2 cycles per second. Typically there is not much tumor motion above a few cycles per second.[2] Therefore, if one wants to reconstruct motion trajectories due to heartbeat and respiration it should be sufficient to take measurements at 3–4 cycles per second, each of 32 ms duration, by pulsing the source. This would reduce the fluoroscopic dose by an order of magnitude from the conventional exposure and make quasi-continuous fluoroscopy a very viable technique for continuous tumor tracking even during single fraction radiosurgery. This type of reduced frame rate capability has been introduced in the second-generation Hokkaido-type system.[71]

However, fluoroscopic sampling of the tumor position must allow for motion of the internal organ that is sometimes unpredictable,[56,89] and the latency between the image acquisition and delivery of therapeutic beam must be short[90] to prevent large errors in compensating the system lag time. This puts limits on the amount of acceptable exposure reduction.

V.C. Nonradiographic imaging and hybrid imaging/tracking

X-ray imaging is not the only way to locate tumors before and during treatment. Nonradiographic localization using implanted electromagnetic transponders has recently been demonstrated[91] and offers an alternative or supplement to x-ray imaging modalities to locate treatment sites that have been marked by implanted fiducials. Although this is an invasive technique that is applicable only to sites into which markers can be placed, it provides continuous position information that allows one to significantly reduce or even eliminate the imaging duty cycle without a loss of position accuracy.

There is also an effort underway to demonstrate magnetic resonance imaging in the treatment room by integrating an MR system with a linac radiation delivery device.[92] If successful, this development will allow not only pretreatment setup using MR, but intrafraction monitoring as well, leaving x-ray techniques for treatment planning (CT) and real-time motion adaptation (fluoroscopy).

VI. SUMMARY AND RECOMMENDATIONS

Image-guided radiotherapy (IGRT) is the new paradigm for external-beam treatment delivery. For the foreseeable future the imaging will be performed primarily with radiographic modalities, which add more radiation dose to the already high dose burden to the patient, in ways that are fundamentally different from the therapy itself. Good medical practice demands that the negative effects of this concomitant dose be reduced as much as possible.

Reduction begins with assessment and so this task group has been concerned primarily with surveying the variety of radiographic imaging techniques currently or prospectively used during radiotherapy. This survey has collected into one place a description of the basic imaging modalities and their typical configurations for IGRT, a summary of approximate doses delivered by each modality as a function of patient characteristics and treatment site, examples of the imaging scenarios currently employed in the treatment process, and an outline of the procedure for computing a composite imaging dose from the various procedures used in a given treatment.

We have attempted to provide enough data for representative IGRT imaging systems to allow the reader to estimate dose for other systems and configurations (present and future) using general scaling principles for x-ray technique (linear in mAs), geometry ($1/r^2$), and other physical parameters. However, some readers may wish to undertake measurements for specific applications. We refer them to the report of AAPM Task Group 8[34] for measuring radiographic entrance skin exposure, mammography exposure, and CTDI, Islam *et al.*[42] for CBCT measurements, and Tremain *et al.*[22] for C-arm fluoroscopy measurements.

The task group recommends that practitioners of IGRT use this survey information to do the following six things:

(1) In all IGRT treatments, compile a complete picture of all of the imaging procedures to be used before, during, and after treatment;
(2) Identify those image-guidance steps that can potentially be accomplished without the use of ionizing radiation;
(3) Configure the image acquisition systems to eliminate dose outside the required FOVs;
(4) Plan the imaging technique to be consistent with the image quality and information needed for the treatment decision being made;
(5) After arriving at an IGRT imaging scenario that eliminates un-needed dose and optimizes the required exposure, use the resources of this report to estimate the total effective imaging dose, from all sources, that the patient will receive;
(6) Evaluate the total dose patient-by-patient using guidelines for estimating stochastic and deterministic risk, with the understanding that the diagnostic imaging community relies on judgment rather than prescription in assessing individual exposure risk.

In conservatively designed IGRT procedures, the added risk associated with imaging dose will usually be negligible. In these cases the final recommendation is to think economically—unused dose identified in one procedure can be spent instead in other procedures where it can add useful information.

For researchers and vendors advancing the technology of IGRT, the task group recommends that each role of imaging in the therapeutic process be analyzed for its dependence on ionizing radiation. X-ray imaging will always be a primary tool in IGRT but dose reduction provides an important incentive to develop and apply alternative target localization methods wherever possible. It is further recommended that strategies for reducing the imaging dose and volume of exposed anatomy be pursued wherever possible, even when they require developing new image acquisition and reconstruction techniques. Vendors should be encouraged to provide pulsed fluoroscopy, adjustable FOV collimation, continuously adjustable LINAC output for portal imaging, and limited FOV CT reconstruction algorithms, etc. The rationale for this is simple—we want to spend only as much imaging dose as is required to effect a net gain in the quality of treatment. If the information requirements of today's IGRT had to be met using the radiographic technologies of 25 years ago, the patient exposure levels would almost certainly be unacceptably high.

Physicists and physicians frequently attempt comparisons of imaging and therapy dose but we have already pointed out that this is problematic when it is done simply by comparing air kerma or CTDI to the treatment dose measured in units of Gy. This is not even appropriate for comparisons among different imaging modalities.[33] Effective dose in mSv is the correct quantity to use for these comparisons, but because treatment scenarios are far more varied than imaging scenarios there have been very few attempts at estimating effective dose from the therapy beam. The task group recommends that the image-guided radiotherapy community investigate calculations of effective dose from the primary and scattered therapy beam so that imaging and therapy dose can be properly compared.

VII. BIBLIOGRAPHIC NOTES

In this final section we collect representative references by topic. This is in no way meant to be a comprehensive survey of the literature.

Dose from radiography[1,17–19,23,24,33–35,49,76,93]
Overview of image-guided radiotherapy[5,70,94–96]
Diagnostic (kV) x-ray imaging for patient setup and tracking[28,97–102]
Breathing motion management[2,6,9,10,58–65,89,103]
Megavoltage portal imaging[20,21,67,104–108]
Intrafraction fluoroscopic imaging[11,51–56,71,90]
Imaging for brachytherapy seed localization[66]
Megavoltage CT during tomotherapy[7,8,87,109–114]
CT use and dosimetry[30–33,36,74,135–138,144]
4D CT[36,139]
CT on rails[140–142]
Kilovoltage cone-beam CT[39–41,43,44,57,69,88,122]
Megavoltage axial and cone-beam CT[38,46,48,111–133]
Dose Measurement[22,34,42,146]
Concomitant dose from the therapy beam[14–16,134,145]
Effective dose[25,26,45,68,73,86,143]
Deterministic injury from fluoroscopy[12,13,22,72,76]

[1]E. G. A. Aird, "Second cancer risk, concomitant exposures, and IRMER(2000)," Br. J. Radiol. **77**, 983–985 (2004).
[2]M. J. Murphy, "Tracking moving organs in real time," Semin. Radiat. Oncol. **14**, 91–100 (2004).

[3]G. S. Mageras, "Management of target localization uncertainties in external-beam therapy," Semin. Radiat. Oncol. **15**, 133–135 (2005).
[4]D. Jaffray, "Emergent technologies for 3-dimensional image-guided radiation delivery," Semin. Radiat. Oncol. **15**, 208–216 (2005).
[5]L. Xing, B. Thorndyke, E. Schreibmann, Y. Yang, T.-F. Li, G.-Y. Kim, G. Luxton, and A. Koong, "Overview of image-guided radiation therapy," Med. Dosim. **31**, 91–112 (2006).
[6]F. J. Lagerwaard *et al.*, "Multiple 'slow' CT scans for incorporating lung tumor mobility in radiotherapy planning," Int. J. Radiat. Oncol., Biol., Phys. **51**, 932–937 (2001).
[7]T. R. Mackie, T. Holmes, S. Swerdloff, P. Reckwerdt, J. O. Deassy, J. Yang, B. Paliwal, and T. Kinsella, "Tomotherapy: A new concept for the delivery of dynamic conformal radiotherapy," Med. Phys. **20**, 1709–1719 (1993).
[8]T. R. Mackie "Helical tomotherapy: Image-guided IMRT," Med. Phys. **29**, 1332–1324 (2002).
[9]T. Bortfeld and G. Chen, "High precision radiation therapy of moving targets," Semin. Radiat. Oncol. **14**, 1–100 (2004).
[10]P. J. Keall, G. S. Mageras, J. M. Balter, R. S. Emery, K. M. Forster, S. B. Jiang, J. M. Kapatoes, D. A. Low, M. J. Murphy, B. R. Murray, C. R. Ramsey, M. B. Van Herk, S. S. Vedam, J. W. Wong, and E. Yorke, "The management of respiratory motion in radiation oncology report of AAPM Task Group 76," Med. Phys. **33**, 3874–3900 (2006).
[11]H. Shirato *et al.*, "Physical aspects of a real-time tumor-tracking system for gated radiotherapy," Int. J. Radiat. Oncol., Biol., Phys. **48**, 1187–1195 (2000).
[12]L. K. Wagner, P. J. Eifel, and R. A. Geise, "Potential biological effects following high x-ray dose interventional procedures," J. Vasc. Interv. Radiol. **5**, 71–81 (1994).
[13]T. B. Shope, "Radiation-induced skin injuries from fluoroscopy," Radiographics **16**, 1195–1199 (1996).
[14]D. Followill, P. Geis, and A. Boyer, "Estimates of whole-body dose equivalent produced by beam intensity-modulated conformal therapy," Int. J. Radiat. Oncol., Biol., Phys. **38**, 667–672 (l997).
[15]E. J. Hall and C. S. Wuu, "Radiation-induced second cancers: The impact of 3D-CRT and IMRT," Int. J. Radiat. Oncol., Biol., Phys. **56**, 83–88 (2003).
[16]D. Brenner, "Induced cancers after prostate-cancer radiotherapy: No cause for concern?" Int. J. Radiat. Oncol., Biol., Phys. **65**, 637–639 (2006).
[17]BEIR, Committee on the Biological Effects of Ionizing Radiations (BEIR V), National, Research Council, "Health effects of exposure to low levels of ionizing radiation: BEIR V" (National Academy Press, Washington, DC, 1990).
[18]D. J. Brenner, "Estimating cancer risks from pediatric CT: Going from the qualitative to the quantitative," Pediatr. Radiol. **32**, 228–231 (2002).
[19]NCRP, "Medical x-ray, electron beam and gamma-ray protection for energies up to 50 MeV (Equipment design, performance and use)," NCRP Report 102, 1989.
[20]L. Beaulieu, L. M. Girouard, S. Aubin, J. F. Aubry, L. Brouard, L. Roy-Lacroix, J. Dumont, D. Trembley, E. Vigneault, and J. Laverdiere, "Performing Daily Prostate Targeting with a Standard V-EPID and an Automated Radio-Opaque Marker Detection Algorithm," Radiother. Oncol. **73**, 61–64 (2004).
[21]L. Wolfsberger, R. Tishler, A. Allen, S. James, J. Killoran, and L. Court, "Importance of Daily Portal Imaging for Head and Neck IMRT Treatments" Med. Phys. **33**, 2039–2039 (2006).
[22]M. R. Tremains, G. M. Georgiadis, and M. J. Dennis, "Radiation exposure with use of the inverted C-arm technique in upper-extremity surgery," J. Bone Jt. Surg. **83A**, 674–768 (2001).
[23]NCRP, "Implementation of the principle of as low as reasonably achievable (ALARA) for medical and dental personnel," NCRP Report 107, 1990.
[24]J. E. Gray *et al.*, "Reference values in diagnostic radiology; application and impact," Radiology **235**, 354–358 (2005).
[25]C. H. McCollough and B. A. Schueler, "Calculation of effective dose," Med. Phys. **27**, 828–837 (2000).
[26]W. Jacobi, "The concept of effective dose: A proposal for the combination of organ doses," J. Radiat. Environ. Biophys. **12**, 101–109 (1975).
[27]F. F. Yin (unpublished, private communication).
[28]C. L. Perkins, T. Fox, E. Elder, D. A. Kooby, C. A. Staley III, and J. Landry, "Image-guided radiation therapy (IGRT) in gastrointestinal tumors," JOP: Journal of the Pancreas (online) **7**, 372–381 (2006).
[29]V. S. Khoo, D. P. Dearnaley, D. J. Finnign, A. Padhani, S. F. Tanner, and M. O. Leach, "Magnetic resonance imaging (MRI): Considerations and applications in radiotherapy treatment planning," Radiother. Oncol. **42**, 1–15 (1997).
[30]I. J. Kalet and M. M. Austin-Seymour, "The use of medical images in planning and delivery of radiation therapy," J. Am. Med. Inform Assoc. **4**, 327–339 (1997).
[31]M. L. Kessler and R. K. Ten Haken, "Use of MRl data for treatment planning," in *Imaging in Radiation Therapy*, edited by J. D. Hazle and A. L. Boyers (Medical Physics Publishing, Madison, WI, 1998), pp. 313–316.
[32]G. A. Ezzell *et al.*, "Guidance document on delivery, treatment planning, and implementation of IMRT, Report of the IMRT subcommittee of the AAPM radiation therapy committee," Med. Phys. **30**, 2089–2115 (2003).
[33]*Radiation Exposure in Computed Tomography*, edited by H. D. Nagel (CTB Publications, Hamburg, Germany, 2002).
[34]R. Y. L. Chu, J. Fisher, B. R. Archer, B. J. Conway, M. M. Goodsitt, S. Glaze, J. E. Gray, and K. J. Strauss, "Standardized methods for measuring diagnostic x-ray exposures," AAPM Report 31, 1990.
[35]S. Diederich and H. Lenzen, "Radiation exposure associated with imaging of the chest: Comparison of different radiographic and computed tomography techniques," Cancer **89**, 2457–2460 (2000).
[36]P. J. Keall *et al.*, "Acquiring 4D thoracic CT scans using a multislice helical method," Phys. Med. Biol. **49**, 2053–2067 (2004).
[37]D. A. Low *et al.*, "A method for the reconstruction of four-dimensional synchronized CT scans acquired during free breathing," Med. Phys. **30**, 1254–1263 (2003).
[38]J. Chen, O. Morin, M. Aubin, M. K. Bucci, C. F. Chuang, and J. Pouliot, Dose-guided radiation therapy with megavoltage cone-beam CT," Br. J. Radiol. **79**, S87–S98 (2006).
[39]D. Jaffray and J. H. Siewerdsen, "Cone-beam computed tomography with a flat-panel imager: Initial performance characterization," Med. Phys. **27**, 1311–1323 (2000).
[40]D. Letourneau, J. Wong, M. Oldham, M. Gulam, L. Watt, D. A. Jaffray, J. H. Siewerdson, and A. A. Martinez, "Cone-beam-guided radiation therapy: Technical implementation," Radiother. Oncol. **75**, 279–286 (2005).
[41]C. Thilmann *et al.*, "Correction of patient positioning errors based on in-line cone beam CTs: Clinical implementation and first experiences," Radiat. Oncol. **1**, 1–16 (2006).
[42]M. K. Islam, T. G. Purdie, B. D. Norrlinger, H. Alasti, D. J. Moseley, M. B. Sharpe, J. H. Siewerdsen, and D. A. Jaffray, "Patient dose from kilovoltage cone beam computed tomography imaging in radiation therapy," Med. Phys. **33**, 1573–1582 (2006).
[43]A. Amer *et al.*, "Doses from cone beam CT integrated to a radiotherapy treatment machine," United Kingdom Radiation Oncology Conference, April 2005.
[44]P. H. Cossmann, A. Stuessl, and C. von Briel, "Cone-beam CT experience in Aarau," ESTRO Workshop on Image-Guided Radiotheraphy, S9, (2005).
[45]M. Endo *et al.*, "Image characteristics and effective dose estimation of a cone-beam CT using a video-fluoroscopic system," IEEE Trans. Nucl. Sci. **46**, 686–690 (1999).
[46]K. Nakagawa, Y. Aoki, M. Tago, A. Terahara, and K. Ohtomo, "Megavoltage CT-assisted stereotactic radiosurgery for thoracic tumors: Original research in the treatment of thoracic neoplasms," Int. J. Radiat. Oncol., Biol., Phys. **48**, 449–457 (2000).
[47]C. H. McCollough and F. E. Zink, "Performance evaluation of a multislice CT system," Med. Phys. **26**, 2223–2230 (1999).
[48]J. Sillanpaa, J. Chang, and G. Mageras, "Developments in megavoltage cone beam CT with an amorphous silicon EPID: Reduction of exposure and synchronization with respiratory gating," Med. Phys. **32**, 819–829 (2005).
[49]J. P. Winston and D. B. Gilley, "Patient Exposure and Dose Guide 2003," Conference of Radiation Control Program Directors, CRCPD publication E-03-2 (2003).
[50]C. J. Moore *et al.*, "Developments in and experience of kilovoltage x-ray cone beam image-guided radiotherapy," J. Radiol. **79**, S66–S78 (2006).
[51]S. Shimizu *et al.*, "Use of an implanted marker and real-time tracking of the marker for the positioning of prostate and bladder cancers," Int. J. Radiat. Oncol., Biol., Phys. **48**, 1591–1597 (2000).
[52]S. Shimizu *et al.*, "Detection of lung tumor movement in real-time tumor-tracking radiotherapy," Int. J. Radiat. Oncol., Biol., Phys. **51** 304–310

(2001).
[53]Y. Seppenwoolde, H. Shirato, K. Kitamura, S. Shimizu, M. van Herk, J. V. Lebesque, and K. Miyasada, "Precise and real-time measurement of 3D tumor motion in lung due to breathing and heartbeat, measured during radiotherapy," Int. J. Radiat. Oncol., Biol., Phys. **53**, 822–834 (2002).
[54]K. Kitamura, H. Shirato, Y. Seppenwoolde, R. Onimaru, M. Oda, K. Fujita, S. Shimizu, N. Shinohara, T. Harabayashi, and K. Miyasaka, "Three-dimensional intrafractional movement of prostate measured during real-time tumor-tracking radiotherapy in supine and prone treatment positions," Int. J. Radiat. Oncol., Biol., Phys. **43**, 1117–1123 (2002).
[55]K. Kitamura, H. Shirato, Y. Seppenwoolde, T. Shimizu, Y. Kodama, H. Endo, R. Onimaru, M. Oda, K. Fujita, S. Shimizu, and K. Miyasaka, "Tumor location, cirrhosis, and operation history contribute to tumor movement in the liver, as measured during stereotactic irradiation using a real-time tumor-tracking radiation therapy system," Int. J. Radiat. Oncol., Biol., Phys. **56**, 221–228 (2003).
[56]H. Shirato, Y. Seppenwoolde, K. Kitamura, R. Onimura, and S. Shimizu, "Intrafractional tumor motion: Lung and liver," Semin. Radiat. Oncol. **14**, 10–18 (2004).
[57]J. H. Siewerdsen and D. A. Jaffray, "Cone-beam computed tomography with a flat-panel imager: Magnitude and effects of x-ray scatter," Med. Phys. **28**, 220–231 (2001).
[58]G. S. Mageras, "Interventional strategies for reducing respiratory-induced motion in external beam therapy," ICCR 2000, Heidelberg, 514–516 (2000).
[59]K. E. Rosenzweig *et al.*, "The deep inspiration breathe-hold technique in the treatment of inoperable non-small-cell lung cancer," Int. J. Radiat. Oncol., Biol., Phys. **48**, 81–87 (2000).
[60]E. A. Barnes, B. R. Murray, D. M. Robinson, L. J. Underwood, J. Hanson, and W. H. Roa, "Dosimetric evaluation of lung tumor immobilization using breath hold at deep inspiration," Int. J. Radiat. Oncol., Biol., Phys. **50**, 1091–1098 (2001).
[61]M. J. Murphy, D. Martin, R. Whyte, C. Ozhasoglu, J. Hai, and Q.-T. Le, "The effectiveness of breathholding to stabilize lung and pancreas tumors during radiosurgery," Int. J. Radiat. Oncol., Biol., Phys. **53**, 475–482 (2002).
[62]J. W. Wong *et al.*, "The use of active breathing control (ABC) to reduce margin for breathing motion," Int. J. Radiat. Oncol., Biol., Phys. **44**, 911–919 (1999).
[63]K. H. Klaus, D. Jurgen, L. Frank, F. Peter, B. Malte, R. Bernhard, M. Johann, K. Jurgan, S. Wolfgang, and W. Michael, "Extracranial stereotactic conformal radiation treatment of tumors in the liver and the lung," Int. J. Radiat. Oncol., Biol., Phys. **42**, 214 (1998).
[64]H. D. Kubo and B. C. Hill, "Respiration gated radiotherapy treatment: A technical study," Phys. Med. Biol. **41**, 83–91 (1996).
[65]A. Schweikard G. Glosser, M. Bodduluri, M. Murphy, and J. R. Adler, "Robotic motion compensation for respiratory movement during radiosurgery," Comput. Aided Surg. **5**, 263–277 (2000).
[66]F. A. Siebert, P. Kohr, and G. Kovacs, "The design and testing of a solid phantom for the verification of a commercial 3D seed reconstruction algorithm," Radiother. Oncol. **74**, 169–175 (2005).
[67]M. Herman, "Clinical use of electronic portal imaging," Semin. Radiat. Oncol. **15**, 157–167 (2005).
[68]S. P. Waddington and A. L. McKensie, "Assessment of effective dose from concomitant exposures required in verification of the target volume in radiotherapy," Br. J. Radiol. **77**, 557–561 (2004).
[69]J. H. Siewerdsen *et al.*, "Volume CT with a flat-panel detector on a mobile, isocentric C-arm: Pre-clinical investigation in guidance of minimally invasive surgery," Med. Phys. **32**, 241–254 (2005).
[70]M. J. Murphy, S. D. Chang, and I. C. Gibbs, "Patterns of patient movement during frameless image-guided radiosurgery," Int. J. Radiat. Oncol., Biol., Phys. **55**, 1400–l408 (2003).
[71]H. Shirato, M. Oita, K. Fujita, Y. Watanabe, and K. Miyasaka, "Feasibility of synchronization of real-time tumor-tracking radiotherapy and intensity-modulated radiotherapy from viewpoint of excessive dose from fluoroscopy," Int. J. Radiat. Oncol., Biol., Phys. **60**, 335–341 (2004).
[72]National Institutes of Health, "Interventional fluoroscopy: Reducing radiation risks for patients and staff," NIH Publication 05-5286 (March, 2005).
[73]J. C. Le Heron, "Estimation of effective dose to the patient during medical x-ray examinations from measurements of the dose-area product," Phys. Med. Biol. **37**, 2117–2126 (1992).
[74]M. Galanski, H. D. Nagel, and G. Stamm, "Expositions-dosis bei CT-untersuchungen: Ergebnisse einer bundesweiten umgfrage," Fortschr. Rontgenstr. **172**, M164–M168 (2000).
[75]E. G. Fiberg, "Norwegian Radiation Protection Authority, Department of Radiation Protection and Nuclear Safety," Østerås, Norway, 193–196 (2000).
[76]ICRP-60, The International Commission on Radiological Protection, *Recommendations on Radiation Protection*, ICRP Publication 60 (Pergamon Press, Oxford, 1991).
[77]S. D. Chang, D. P. Martin, and J. R. Adler, "Treatment of spinal AVMs and vascular tumors with frameless image-based radiosurgery," J. Neurosurg. **88**, 201A (1998).
[78]S. D. Chang, M. Marcellus, M. P. Marks, R. P. Levy, H. M. Do, and G. K. Steinberg, "Multimodality treatment of giant intracranial arteriovenous malformations," Neurosurgery **53**, 1–14 (2003).
[79]J. C. Flickinger, D. Kondziolka, A. Niranjan, and L. D. Lunsford, "Results of acoustic neuroma radiosurgery: An analysis of 5 years experience using current methods," J. Neurosurg. **94**, 1–6 (2001).
[80]M. Lim, A. T. Villavicencio, S. Burneikiene, S. D. Chang, P. Romanell, L. Mcneely, M. McIntyre, J. J. Thramann, and J. R. Adler, "Cyber knife radiosurgery for idiopathic trigeminal neuralgia," Neurosurg. Focus **18**, article E9, 1–7 (2005).
[81]M. Mitsumori, D. C. Shrieve, E. Alexander III, U. B. Kaiser, G. E. Richardson, P. M. Black, and J. S. Loeffler, "Initial clinical results of Linac-based stereotactic radiosurgery and stereotactic radiotherapy for pituitary adenomas," Int. J. Radiat. Oncol., Biol., Phys. **42**, 573–580 (1998).
[82]P. N. Plowman, "Pituitary adenoma radiotherapy—when, who and how," Clin. Endocrinol. **51**, 265–271 (1999).
[83]J. P. Sheehan, D. Kondziolka, J. Flicklinger, and L. D. Lundsford, "Radiosurgery for residual and recurrent nonfunctioning pituitary adenoma," J. Neurosurg. **97**, 408–414 (2002).
[84]I. Diallo, A. Lamon, A. Shamsaldin, E. Grimaud, F. de Vathaire, and J. Chavaudra, "Estimation of the radiation dose delivered to any point outside the target volume per patient treated with external beam radiotherapy," Radiother. Oncol. **38**, 269–271 (1996).
[85]A. A. Cigna, D. Nassisi, D. Masenga, R. Raffo, and P. Rotta, "Dose due to scattered radiation in external radiotherapy: A prostate cancer case history," Radiat. Prot. Dosim. **108**, 27–32 (2004).
[86]H. Ing, W. R. Nelson, and R. A. Shore, "Unwanted photon and neutron radiation resulting from collimated photon beams interacting with the body of radiotherapy patients," Med. Phys. **9**, 27–33 (1982).
[87]K. Sheng, R. Jeraj, R. Shaw, T. R. Mackie, and B. R. Paliwal, "Imaging dose management using multi-resolution in CT-guided radiation therapy," Phys. Med. Biol. **50**, 1205–1219 (2005).
[88]M. Oldham, D. Letourneau, L. Watt, G. Hugo, D. Yan, D. Lockman, L. H. Kim, P. Y. Chen, A. Martinez, and J. W. Wong, "Cone-beam-T-guided radiation therapy: A model for on-line application," Radiother. Oncol. **75**, 271–278 (2005).
[89]C. Ozhasoglu and M. J. Murphy, "Issues in respiratory motion compensation during external-beam radiotherapy," Int. J. Radiat. Oncol., Biol., Phys. **52**, 1389–1399 (2002).
[90]G. C. Sharp, S. B. Jiang, S. Shimizu, and H. Shirato, "Prediction of respiratory tumour motion for real-time image-guided radiotherapy," Phys. Med. Biol. **49**, 425–440 (2004).
[91]J. M. Balter *et al.*, "Accuracy of a wireless localization system for radiotherapy," Int. J. Radiat. Oncol., Biol., Phys. **6l**, 933–937 (2005).
[92]B. W. Raaymakers *et al.*, "Integrating a MRI scanner with a radiotherapy accelerator: A new concept of precise on-line radiotherapy guidance and treatment monitoring," *14th Proceedings International Conference on the Use of Computers in Radiation Therapy* (Seoul, South Korea), pp. 89–92 (2004).
[93]D. Hart and B. F. Wall, "Radiation exposure of the UK population from medical and dental x-ray examinations," National Radiological Protection Board NRPb-W4 (2002).
[94]L. Bruni, S. Lavalle, J. Troccaz, P. Cinquin, and M. Bolla, "Pre-and intra-irradiation multi-modal image registration: Principles and first experiments," Radiother. Oncol. **29**, 244–252 (1993).
[95]H. Geinitz, F. B. Zimmermann, A. Kuzmany, and P. Knechaurek, "Daily CT planning during boost irradiation of prostate cancer: feasibility and time requirements," Strahlenther. Onkol. **176**, 429–432 (2000).
[96]D. L. VandenBerge, M. DeRidder, and G. A. Storme, "Imaging in radiotherapy," Eur. J. Radiol. **36**, 41–48 (2000).
[97]J. R. Adler, M. J. Murphy, S. D. Chang, and S. L. Hancock, "Image-guided robotic radiosurgery," Neurosurgery **44**, 1299–1307 (1999).

[98]J. M. Balter *et al.*, "Daily targeting of intrahepatic tumors for radiotherapy," Int. J. Radiat. Oncol., Biol., Phys. **52**, 266–271 (2002).
[99]M. J. Murphy, J. R. Adler, M. Bodduluri, J. Dooley, K. Forster, J. Hai, Q. Le, G. Luxton, D. Martin, and J. Poen, "Image-guided radiosurgery for the spine and pancreas," Comput. Aided Surg. **5**, 278–288 (2000).
[100]L. J. Pisani, D. A. Jaffray, D. Lockman, D. Yan, and J. W. Wong, "A mega- and kilo-voltage radiographic guidance system: Calibration and clinical implementation," *EPI98 International Workshop on Electronic Portal Imaging*, pp. 89–90 (1998).
[101]J. E. Schewe, K. L. Lam, J. M. Balter, and R. K. TenHaken, "A room-based diagnostic imaging system for measurement of patient setup," Med. Phys. **25**, 2385–2387 (1998).
[102]F. F. Yin *et al.*, "A technique of intensity-modulated radiosurgery (IMRS) for spinal tumor," Med. Phys. **29**, 2815–2822 (2002).
[103]P. J. Keall, V. R. Kini, S. Vedam, and R. Mohan, "Motion adaptive x-ray therapy: A feasibility study," Phys. Med. Biol. **46**, 1–10 (2000).
[104]L. E. Antonuk and Y. El-Mohri, "Active matrix flat-panel imagers for electronic portal imaging," in *Imaging in Radiotherapy*, edited by J. D. Hazle and A. L. Boyer, AAPM Summer School, 1998.
[105]G. S. Mageras and G. J. Kutcher, "The role of EPIDs in conformal therapy," in *Imaging in Radiotherapy*, edited by J. D. Hazle and A. L. Boyer, AAPM Summer School, 1998.
[106]K. G. A. Gilhuijs, P. J. H. vandeVen, and M. vanHerk, "Automatic three-dimensional inspection of patient setup in radiation therapy using portal images, simulator images, and computed tomography data," Med. Phys. **23**, 389–399 (1996).
[107]K. G. A. Gilhuijs, K. Drukker, A. Touw, P. J. H. van deVen, and M. van Herk, "Interactive three-dimensional inspection of patient setup in radiation therapy using digital portal images and computed tomography data," Int. J. Radiat. Oncol., Biol., Phys. **34**, 873–885 (1996).
[108]H. Meertens, M. van Herk, and J. Weeda, "A liquid ionization detector for digital radiography of therapeutic megavoltage photon beams," Phys. Med. Biol. **30**, 313–321 (1985).
[109]E. E. Fitchard, J. S. Aldridge, K. Ruchala, G. Fang, J. Balog, D. W. Pearson, G. H. Olivera, E. A. Schloesser, D. Wenman, P. J. Reckwerdt, and T. R. Mackie, "Registration using tomographic projection files," Phys. Med. Biol. **44**, 495–507 (1999).
[110]E. E. Fitchard, J. S. Aldridge, P. J. Reckwerdt, G. H. Olivera, T. R. Mackie, and A. Iosevich, "Six parameter patient registration directly from projection data," Nucl. Instrum. Methods Phys. Res. A **A421**, 342–351 (1999).
[111]B. Hesse, L. Spies, and B. Groh, "Tomotherapeutic portal imaging for radiation treatment verification," Phys. Med. Biol. **43**, 3607–3616 (1998).
[112]K. J. Ruchala, G. H. Olivera, E. A. Schloesser, and T. R. Macki, "Megavoltage CT on a tomotherapy system," Phys. Med. Biol. **44**, 2597–2621 (1999).
[113]K. J. Ruchala, G. H. Olivera, J. M. Kapatoes, E. A. Schloesser, P. J. Reckwerd, and T. R. Mackie, "Megavoltage CT image reconstruction during tomotherapy treatments," Phys. Med. Biol. **45**, 3545–3562 (2000).
[114]K. J. Ruchala, G. H. Olivera, J. M. Kapatoes, E. A. Schloesser, P. J. Reckwerdt, and T. R. Mackie, "Megavoltage CT imaging as a by-product of multileaf collimator leakage," Phys. Med. Biol. **45**, N61–N70 (2000).
[115]E. Seppi *et al.*, "Megavoltage cone-beam computed tomography using a high quantum efficiency image receptor," Int. J. Radiat. Oncol., Biol., Phys. **55**, 793–803 (2003).
[116]J. Pouliot *et al.*, "Low-dose megavoltage cone-beam CT for radiation therapy," Int. J. Radiat. Oncol., Biol., Phys. **61**, 552–560 (2005).
[117]E. C. Ford *et al.*, "Cone-beam CT with megavoltage beams and an amorphous silicon electronic portal imaging device: Potential for verification of radiotherapy of lung cancer," Med. Phys. **29**, 2913–2924 (2002).
[118]G. Pang and J. A. Rowlands, "Development of high quantum efficiency, flat panel, thick detectors for megavoltage x-ray imaging: A novel direct-conversion design and its feasibility," Med. Phys. **31**, 3004–3016 (2004).
[119]B. A. Groh, J. H. Siewerdsen, D. G. Drake, J. W. Wong, and D. A. Jaffray, "MV and kV cone-beam CT on a medical linear accelerator," in *ICCR: The use of computers in radiation therapy*, edited by W. Schlegel and T. Bortfeld (Springer Verlag, Heidelberg, 2000), pp. 561–563.
[120]B. A. Groh, J. H. Siewerdsen, D. G. Drake, J. W. Wong, and D. A. Jaffray, "A performance comparison of flat-panel imager-based MV and KV cone-beam CT," Med. Phys. **29**, 967–975 (2002).
[121]S. Loose and K. W. Leszczynski, "On few-view tomographic reconstruction with megavoltage photon beams," Med. Phys. **28**, 1679–1688 (2001).
[122]J. Siewerdsen and D. Jaffray, "NEQ description of 3D imaging performance in flat-panel cone-beam CT," Med. Phys. **29**, 1321–1321 (2002).
[123]Y. Aoki, A. Akanuma, P. M. Evans, D. G. Lewis, E. J. Morton, and W. Swindell, "A dose distribution evaluation utilizing megavoltage CT imaging system," Radiat. Med. **8**, 107–110 (1990).
[124]A. Brahme, B. Lind, and P. Nafstadius, "Radiotherapeutic computed tomography with scanned photon beams," Int. J. Radiat. Oncol., Biol., Phys. **13**, 95–101 (1987).
[125]H. Guan and Y. Zhu, "Feasibility of megavoltage portal CT using an electronic portal imaging device (EPID) and a multi-level scheme algebraic reconstruction technique," Phys. Med. Biol. **43**, 2925–2937 (1998).
[126]D. G. Lewis, W. Swindell, E. J. Morton, P. M. Evans, and Z. R. Xiao, "A megavoltage CT scanner for radiotherapy verification," Phys. Med. Biol. **37**, 1985–1999 (1992).
[127]S. Midgley, R. Millar, and J. Dudson, "A feasibility study for megavoltage cone beam CT using a commercial EPID," Phys. Med. Biol. **43**, 155–169 (1998).
[128]M. Mosleh-Shirazi, P. Evans, W. Swindell, S. Webb, and M. Partridge, "A cone-beam megavoltage CT scanner for treatment verification in conformed radiotherapy," Radiother. Oncol. **48**, 319–328 (1998).
[129]M. Partridge, P. M. Evans, and M. A. Mosley-Shirazi, "Linear accelerator output variations and their consequences for megavoltage imaging," Med. Phys. **25**, 1443–1452 (1998).
[130]R. G. T. Simpson, C. T. Chen, E. A. Grubbs, and W. Swindell, "A 4-MV CT scanner for radiation therapy: The prototype system," Med. Phys. **9**, 574–579 (1982).
[131]L. Spies, M. Ebert, B. Groh, B. Hesse, and T. Bortfeld, "Correction of scatter in megavoltage cone-beam CT," Phys. Med. Biol. **46**, 821–833 (2001).
[132]W. Swindell, "A 4-MV CT scanner for radiation therapy: Spectral properties of the therapy beam," Med. Phys. **10**, 347–351 (1983).
[133]W. Swindell, R. G. Simpson, and J. R. Oleson, "Computed tomography with a linear accelerator with radiotherapy applications," Med. Phys. **10**, 416–420 (1983).
[134]S. Mutic and D. A. Low, "Whole-body dose from tomotherapy delivery," Int. J. Radiat. Oncol., Biol., Phys. **42**, 229–232 (1998).
[135]European Guidelines on Quality Criteria for Computed Tomography (http://www.drs.dk).
[136]A. Suzuki and M. N. Susuki, "Use of a pencil-shaped ionization chamber for measurement of exposure resulting from a computed tomography scan," Med. Phys. **5**, 536–539 (1978).
[137]P. C. Shrimpton *et al.*, "Survey of CT practice in the UK: Part 2; Dosimetric aspects," National Radiological Protection Board Report R-249, London: HMSO (1991).
[138]M. F. McNitt-Gray, "Radiation Dose in CT," Radiographics **22**, 1541–1553 (2002).
[139]E. C. Ford *et al.*, "Respiration-correlated spiral CT: A method of measuring respiratory-induced anatomic motion for radiation treatment planning," Med. Phys. **30**, 88–97 (2003).
[140]L. Court *et al.*, "Evaluation of mechanical precision and alignment uncertainties for an integrated CT/LINAC system," Med. Phys. **30**, 1198–1209 (2003).
[141]C. W. Cheng, J. R. Wong, L. Grimm, M. Chow, and M. Uematsu, "Commissioning and clinical implementation of a CT scanner installed in an existing treatment room for precise tumor localization and early clinical experience," Am. J. Clin. Oncol. **26**, e28–e36 (2003).
[142]J. Wong *et al.*, "Image-guided radiotherapy for prostate cancer by CT-linear accelerator combination: Prostate movements and dosimetric considerations," Int. J. Radiat. Oncol., Biol., Phys. **61**, 561–569 (2005).
[143]R. D. Nawfel, P. F. Judy, A. R. Schleipman, and S. G. Silverman, "Patient radiation dose at CT urography and conventional urography," Radiology **232**, 126–132 (2004).
[144]R. L. Morin, T. C. Gerber, and C. H. McCollough, "Radiation dose in computed tomography of the heart," Circulation **107**, 917–922 (2003).
[145]C. S. Reft, R. Runkel-Muller, and L. Myrianthopoulos, "In vivo and phantom measurements of the secondary photon and neutron doses for prostate patients undergoing 18 MV IMRT," Med. Phys. **33**, 3734–3742 (2006).
[146]P. Lin *et al.*, "Protocols for the radiation safety surveys of diagnostic radiological equipment," AAPM Report No. 21988.